

ICES REPORT 12-12

March 2012

Isogeometric Analysis of the Advective Cahn-Hilliard Equation: Spinodal Decomposition Under Shear Flow

by

J. Liu, L. Dede, J.A. Evans, M.J. Borden, T.J.R. Hughes



The Institute for Computational Engineering and Sciences
The University of Texas at Austin
Austin, Texas 78712

Reference: J. Liu, L. Dede, J.A. Evans, M.J. Borden, T.J.R. Hughes, Isogeometric Analysis of the Advective Cahn-Hilliard Equation: Spinodal Decomposition Under Shear Flow, ICES REPORT 12-12, The Institute for Computational Engineering and Sciences, The University of Texas at Austin, March 2012.

Isogeometric Analysis of the Advective Cahn-Hilliard Equation: Spinodal Decomposition Under Shear Flow

Ju Liu*, Luca Dedè†, John A. Evans, Michael J. Borden,
and Thomas J.R. Hughes

Institute for Computational Engineering and Sciences
The University of Texas at Austin
1 University Station C0200
Austin, TX 78712-0027, U.S.A.

Abstract

We present a numerical study of the spinodal decomposition of a binary fluid undergoing shear flow using the advective Cahn-Hilliard equation, a stiff, nonlinear, parabolic equation characterized by the presence of fourth-order spatial derivatives. Our numerical solution procedure is based on isogeometric analysis, an approximation technique for which basis functions of high-order continuity are employed. These basis functions allow us to directly discretize the advective Cahn-Hilliard equation without resorting to a mixed formulation. We present steady state solutions for rectangular domains in two-dimensions and, for the first time, in three-dimensions. We also present steady state solutions for the two-dimensional Taylor-Couette cell. To enforce periodic boundary conditions in this curved domain, we derive and utilize a new periodic Bézier extraction operator. We present an extensive numerical study showing the effects of shear rate, surface tension, and the geometry of the domain on the phase evolution of the binary fluid. Existing theoretical and experimental results support the validity of our simulations.

Key words. Cahn-Hilliard equation; spinodal decomposition; shear flow; steady state; isogeometric analysis; Bézier extraction.

*Corresponding author. E-mail: liujuy@gmail.com, Phone:+1 512 475 6399

†Present address: EPFL SB MATHICSE CMCS, MA C2 557 (Bâtiment MA), Station 8, CH-1015, Lausanne, Switzerland.

1 Introduction

Spinodal decomposition describes the process of phase transformation by which a quenched homogeneous mixture spontaneously separates into distinct phases [12]. The problem of spinodal decomposition under shear flow is of great industrial importance, and many experiments have been conducted to understand shear-driven spinodal decomposition in metallic alloys [52], binary liquid mixtures [11], and polymer blends [22, 35]. Of particular interest are the possible existence of steady states and the dependence of the morphology of steady state patterns on shear rate and geometry. Existing studies have shown that steady states exist and have an anisotropic structure under shear flow. In particular, under quench and steady uniform shear flow, a homogeneous mixture separates into two distinct phases and forms a banded/string structure stretched along the flow direction [35]. The average diameter of the phase bands is reported to decrease with an increase of the shear rate [22].

The Cahn-Hilliard equation is a stiff, nonlinear, parabolic equation which is often used to describe the spinodal decomposition of a binary fluid [12]. As a type of diffuse-interface model [2], the Cahn-Hilliard equation models interfaces between distinct phases as sharp but smooth transition regions where surface tension forces are distributed. The Cahn-Hilliard equation describes the process of dissipation of the Ginzburg-Landau free energy in mass conservative systems [13, 14]. Two competing mechanisms dominate the evolution of a solution to the Cahn-Hilliard equation: minimization of the chemical free energy drives the solution to binodal points and separates the phases while minimization of the interface free energy effectively coarsens the phases. It has been shown that steady state solutions of the Cahn-Hilliard equation converge to the solution of the isoperimetric problem under an appropriate rescaling [47, 59].

The advective Cahn-Hilliard equation introduces an advection term in the Cahn-Hilliard equation to represent the forced flow field. It is frequently used to model spinodal decomposition under shear flow. In this setting, due to the interactions between coarsening processes and the break-up mechanism on the phases induced by the shear flow, the Ginzburg-Landau free energy no longer represents a Lyapunov functional. Therefore, the morphology of steady-state solutions to the advective Cahn-Hilliard equation exhibit interesting patterns under different conditions (shear rate, material surface tension, etc.).

Several numerical experiments [9, 16, 37, 48, 55, 57] have been conducted to simulate the spinodal decomposition under steady uniform shear flow. However, steady state solutions have been obtained for only a limited number of two-dimensional cases [37, 55], and only early time simulations have been performed in three-dimensions [3, 54]. This is due in part to the complicated nature of the advective Cahn-Hilliard equation and also to the limitations of traditional numerical methods (compact finite difference schemes, mixed finite element method, explicit time integration, etc.).

Recently, isogeometric analysis [18, 41] has emerged as a powerful design and analysis tool. It was originally introduced to integrate the fields of Computer Aided Design (CAD) and Computer Aided Engineering (CAE) by directly utilizing the basis functions representing a CAD design within engineering analysis. However, isogeometric analysis also enables us

to produce globally C^k -continuous, $k \geq 1$, basis functions, which is not a trivial task in the context of traditional finite elements [53]. This allows us to directly discrete the fourth-order advective Cahn-Hilliard equation without resorting to mixed formulation [24] or non-conforming elements [27, 58]. Furthermore, isogeometric analysis possesses other advantages over traditional finite element methods in terms of numerical approximation accuracy [6, 28], mesh refinement [19] and robustness [45]. The combination of these properties with the exact representation of NURBS geometries appears to be particularly effective in the approximation of the Cahn-Hilliard equation.

In addition to the challenges presented by the presence of fourth-order derivatives, the Cahn-Hilliard equation is a particularly stiff system. This imposes a prohibitively strict restriction on the time step size for explicit methods. While semi-implicit schemes without such restrictions have been developed [36, 38, 39], they are limited to cases of constant mobility which are not thermodynamically consistent. In order to avoid these complications, we use the fully implicit generalized- α method [17, 44]. To accommodate for the many time scales spanned by the solution of the Cahn-Hilliard equation, we employ an adaptive time stepping scheme. It has been previously shown that, with this scheme, computation time is greatly reduced without sacrificing solution accuracy [31, 33]. Adaptive time stepping is critical for long-time simulations.

For purposes of implementation, we employed the Bézier extraction for NURBS presented in [8]. Indeed, in this framework, the implementation of an isogeometric analysis code can be easily developed from an existing finite element code since the Bézier data structures and, specifically, the Bézier extraction operators allow a local representation of globally smooth NURBS basis functions in terms of C^0 -continuous Bézier (finite) elements. In view of the strong enforcement of periodic boundary conditions in the Taylor-Couette cell, we introduce the notion of a periodic transformation operator for a NURBS basis and we derive the associated periodic Bézier extraction operator. This extraction operator allows for the strong imposition of periodic boundary conditions simply by updating the existing “destination array” denoted ID, which is a typical data structure used in finite elements codes [40].

The rest of this paper is organized as follows. In section 2, we review the advective Cahn-Hilliard model for spinodal decomposition under shear flow. Section 3 deals with the numerical techniques we use to solve the equation. In section 4, we discuss the strong imposition of the essential boundary conditions for the Cahn-Hilliard equation, with particular emphasis on periodic boundary conditions. In section 5, we present and discuss the numerical results. We draw conclusions in section 6. In appendices A, B, and C, we describe the theory and construction methods used for the periodic Bézier extraction operator and present the localized periodic Bézier extraction operator for NURBS bases of degree $p = 1, 2, 3$.

2 The advective Cahn-Hilliard equation

In this section, we recall the advective Cahn-Hilliard equation as a passive two-phase fluid model.

2.1 Derivation of the governing equation

Let $\Omega \subset \mathbb{R}^n$ be an arbitrary open domain, with $n = 2$ or 3 . The boundary of Ω is denoted as Γ and assumed to be sufficiently smooth (e.g., Lipschitz). The outward directed unit vector normal to Γ is denoted as \mathbf{n} . A binary mixture is contained in Ω and $c = c(\mathbf{x}, t) : \Omega \times [0, T) \rightarrow \mathbb{R}$ denotes the concentration of one of its components. The flux of c through Γ is denoted as \mathbf{J} . The concentration c is conserved in the sense that:

$$\frac{D}{Dt} \int_{\Omega} c \, d\Omega = \int_{\Gamma} -\mathbf{J} \cdot \mathbf{n} \, d\Gamma, \quad (2.1)$$

where $\frac{D}{Dt}$ indicates the material time derivative. By applying the divergence and Reynolds' transport theorems, we obtain:

$$\frac{\partial c}{\partial t} + \nabla \cdot (\mathbf{u}c) = -\nabla \cdot \mathbf{J}. \quad (2.2)$$

Above, \mathbf{u} denotes the advective velocity field, and we assume henceforth that \mathbf{u} is divergence-free ($\nabla \cdot \mathbf{u} = 0$). Then, (2.2) can be rewritten as:

$$\frac{\partial c}{\partial t} + \mathbf{u} \cdot \nabla c = -\nabla \cdot \mathbf{J}. \quad (2.3)$$

In order to close our model, we need a constitutive relation to describe the flux \mathbf{J} . According to Fick's law, the flux \mathbf{J} can be written as:

$$\mathbf{J} = -M_c \nabla \left(\frac{\delta \Psi}{\delta c} \right). \quad (2.4)$$

where M_c is a mobility term, Ψ is the specific free energy, and $\frac{\delta \Psi}{\delta c}$ indicates its Fréchet derivative. For simplicity, the mobility term is often assumed to be constant [26, 56]. However, for a thermodynamically consistent model of spinodal decomposition [12], we require the mobility to depend on the mixture concentration. Specifically, we take:

$$M_c = M_0 c(1 - c), \quad (2.5)$$

where M_0 is a chosen positive constant. Such a mobility is commonly referred to as a degenerate mobility. The specific free energy is split into two parts:

$$\Psi = \Psi_c + \Psi_s, \quad (2.6)$$

where Ψ_c is the chemical free energy and Ψ_s is the surface free energy. According to the theory of Cahn and Hilliard [13, 31] for isothermal binary mixtures, the chemical free energy takes the form:

$$\Psi_c = \frac{1}{2\theta} (c \log(c) + (1 - c) \log(1 - c)) + c(1 - c), \quad (2.7)$$

while the surface free energy is given by:

$$\Psi_s = \frac{1}{2}\lambda \nabla c \cdot \nabla c. \quad (2.8)$$

The chemical free energy Ψ_c models the immiscibility of the mixture's two components. It is assumed to take the form of a double well with respect to the concentration c below the critical temperature (the lowest temperature at which the two phases attain the homogeneous mixture state) and a single well above the critical temperature. The parameter θ denotes the ratio between the critical temperature and the absolute temperature. Since we are interested in modeling binary mixtures under quench, we assume throughout that $\theta > 1$. More specifically, following [31, 58], the parameter θ is taken to be $3/2$ in all of our simulations. The surface free energy Ψ_s models the attractive long-ranged interactions between molecules of the binary mixture [2]. The parameter λ is a positive constant such that the length scale of the interface thickness is proportional to $\sqrt{\lambda}$.

For appropriate boundary conditions (e.g., $\lambda \nabla c \cdot \mathbf{n} = 0$ on Γ), we can write the variation of the free energy Ψ (Fréchet derivative) as:

$$\frac{\delta \Psi}{\delta c} = \mu_c - \lambda \Delta c, \quad (2.9)$$

where:

$$\mu_c := \frac{d\Psi_c}{dc} = \frac{1}{2\theta} \log\left(\frac{c}{1-c}\right) + 1 - 2c \quad (2.10)$$

is the chemical potential. The governing equation for our binary mixture can then be explicitly written as:

$$\frac{\partial c}{\partial t} + \mathbf{u} \cdot \nabla c = \nabla \cdot (M_c \nabla (\mu_c - \lambda \Delta c)). \quad (2.11)$$

This is the advective Cahn-Hilliard equation.

Remark 1. *We note that the degenerate mobility (2.5) enhances the diffusion process in the interface regions. This enhanced interface diffusion has been observed experimentally. Analytical and numerical studies of the Cahn-Hilliard equation with degenerate mobility can be found in [4, 25, 31].*

Remark 2. *The standard Cahn-Hilliard equation for $\mathbf{u} = \mathbf{0}$ in (2.11) governs the gradient flow of the total free energy or Lyapunov functional Ψ (2.6) [29]. It describes the evolution in time of total free energy to a local minimum, while conserving the mass. The expression of total free energy (2.6) can be generalized by adding other types of energy. See, for example, [15, 21, 60].*

Remark 3. *The advective Cahn-Hilliard equation (2.11) represents a passive Cahn-Hilliard fluid model in which the advection field is externally imposed. Alternatively, one may consider a full active Cahn-Hilliard fluid model in which the Cahn-Hilliard phase-field model is coupled with the Navier-Stokes equations; see for example [2, 3, 9, 23, 34, 42, 46, 48]. The full active Cahn-Hilliard fluid model is not considered in this work.*

For the advective Cahn-Hilliard equation, we consider the initial condition:

$$c(\mathbf{x}, 0) = c_0(\mathbf{x}) \quad \forall \mathbf{x} \in \Omega, \quad (2.12)$$

which, by dropping the explicit dependence on the space variable \mathbf{x} , reads $c(0) = c_0$ with $c_0 : \Omega \rightarrow \mathbb{R}$. We partition the boundary Γ into the following non-overlapping subdivisions:

$$\Gamma_s := \{\mathbf{x} \in \Gamma \mid \mathbf{u}(\mathbf{x}) \cdot \mathbf{n}(\mathbf{x}) = 0\}, \quad (2.13)$$

$$\Gamma_{in} := \{\mathbf{x} \in \Gamma \mid \mathbf{u}(\mathbf{x}) \cdot \mathbf{n}(\mathbf{x}) < 0\}, \quad (2.14)$$

$$\Gamma_{out} := \{\mathbf{x} \in \Gamma \mid \mathbf{u}(\mathbf{x}) \cdot \mathbf{n}(\mathbf{x}) > 0\}, \quad (2.15)$$

depending on the advective field \mathbf{u} . On Γ_s , we impose the essential no-flux boundary condition $\nabla c \cdot \mathbf{n} = 0$ to mimic the presence of a rigid wall, as well as the natural boundary condition $M_c \nabla \mu_c \cdot \mathbf{n} = 0$ emanating from the fourth-order operator. On Γ_{in} and Γ_{out} , we impose periodic boundary conditions in order to simulate a periodic structure along the flow direction determined by \mathbf{u} . We notice that, in order to impose such boundary conditions in a compatible manner, we require the boundary Γ_{out} to be obtained by means of a rigid body rotation and translation of Γ_{in} . With the above assumptions, the strong form of the advective Cahn-Hilliard problem can be written as follows:

$$\begin{aligned} \frac{\partial c}{\partial t} + \mathbf{u} \cdot \nabla c &= \nabla \cdot (M_c \nabla (\mu_c - \lambda \Delta c)) && \text{in } \Omega \times [0, T], \\ M_c \nabla \mu_c \cdot \mathbf{n} &= 0 && \text{on } \Gamma_s \times [0, T], \\ M_c \lambda \nabla c \cdot \mathbf{n} &= 0 && \text{on } \Gamma_s \times [0, T], \\ c|_{\Gamma_{in}} &= c|_{\Gamma_{out}} && \text{on } \Gamma_{in} \cup \Gamma_{out} \times [0, T], \\ \nabla c \cdot \mathbf{n}|_{\Gamma_{in}} &= -\nabla c \cdot \mathbf{n}|_{\Gamma_{out}} && \text{on } \Gamma_{in} \cup \Gamma_{out} \times [0, T], \\ c(0) &= c_0 && \text{in } \Omega. \end{aligned} \quad (2.16)$$

2.2 Dimensionless form of the advective Cahn-Hilliard equation

We employ a dimensionless form of the advective Cahn-Hilliard equation in the numerical simulations. Let us introduce the following non-dimensional space, time, mobility, and velocity variables, which we denote with the superscript $*$:

$$x^* = x/L_0, \quad t^* = t/T_0, \quad M_c^* = M_c/M_0, \quad \mathbf{u}^* = \mathbf{u}/U_0. \quad (2.17)$$

Above, L_0, T_0, M_0 and U_0 denote the characteristic length, time, mobility and velocity quantities, respectively. Since we have defined the concentration c and the chemical potential μ_c as dimensionless quantities, we have:

$$c^* = c, \quad \mu_c^* = \mu_c. \quad (2.18)$$

Hence, in dimensionless variables, the advective Cahn-Hilliard equation (2.11) becomes:

$$\mathbb{N}_1 \frac{\partial c^*}{\partial t^*} + \mathbb{N}_3 \mathbf{u}^* \cdot \nabla^* c^* = \nabla^* \cdot \left(M_c^* \nabla^* (\mathbb{N}_2 \mu_c^* - \Delta^* c^*) \right), \quad (2.19)$$

where the dimensionless parameters \mathbb{N}_i , for $i = 1, 2, 3$, are defined as:

$$\mathbb{N}_1 := \frac{L_0^4}{M_0 \lambda T_0}, \quad \mathbb{N}_2 := \frac{L_0^2}{\lambda}, \quad \mathbb{N}_3 := \frac{L_0^3 U_0}{M_0 \lambda}. \quad (2.20)$$

If we choose the characteristic time scale as $T_0 = \frac{L_0^4}{\lambda M_0}$, we have $\mathbb{N}_1 = 1$. Additionally, by recalling the definition of the Péclet number $\mathbb{P}e$:

$$\mathbb{P}e := \frac{U_0 L_0}{M_0}, \quad (2.21)$$

we notice that:

$$\mathbb{N}_3 = \mathbb{N}_2 \mathbb{P}e. \quad (2.22)$$

For the sake of simplicity, we will henceforth omit the superscript $*$ for the dimensionless quantities and we will consider the following form of the dimensionless advective Cahn-Hilliard equation:

$$\frac{\partial c}{\partial t} + \mathbb{N}_2 \mathbb{P}e \mathbf{u} \cdot \nabla c = \nabla \cdot \left(M_c \nabla (\mathbb{N}_2 \mu_c - \Delta c) \right). \quad (2.23)$$

Notice that the above equation is completely characterized by the dimensionless parameter \mathbb{N}_2 and the Péclet number $\mathbb{P}e$. In the remainder of this paper, the advective field \mathbf{u} will represent a shear induced flow field. It follows that the characteristic quantity U_0 may be expressed in terms of a shear rate γ :

$$U_0 = \gamma L_0. \quad (2.24)$$

Hence, we can express the Péclet number in terms of the shear rate γ as:

$$\mathbb{P}e = \frac{\gamma L_0^2}{M_0}. \quad (2.25)$$

3 Numerical formulation

In this section we discuss the numerical procedure for the solution of the advective Cahn-Hilliard equation using NURBS-based isogeometric analysis. Our approach is similar to the one described in [31, 33]; see also [21] for further details. Standard notation is used to denote the Sobolev spaces and norms; see for example [1].

3.1 Weak form of the problem

We start by considering the weak form the advective Cahn-Hilliard equation.

Let us denote by \mathcal{V} the trial solution and weighting function spaces, which we assume are coincident. Due to the presence of the fourth-order operator in the Cahn-hilliard equation and the essential boundary conditions (2.16), we select:

$$\mathcal{V} := \{v \in \mathcal{H}^2(\Omega) : v|_{\Gamma_{in}} = v|_{\Gamma_{out}}, \nabla v \cdot \mathbf{n}|_{\Gamma_{in}} = -\nabla v \cdot \mathbf{n}|_{\Gamma_{out}}, \nabla v \cdot \mathbf{n}|_{\Gamma_s} = 0\}. \quad (3.1)$$

The variational formulation reads:

$$\begin{aligned} \text{find } c(t) \in \mathcal{L}^2(0, T; \mathcal{V}) \cap \mathcal{H}^1(0, T; \mathcal{L}^2(\Omega)) : \\ B(w; \dot{c}(t), c(t)) = 0 \quad \forall w \in \mathcal{V}, \quad t \in [0, T), \\ \text{with } c(0) = c_0 \quad \text{in } \Omega, \end{aligned} \quad (3.2)$$

where, by dropping the dependence of c on t , indicating with $(\cdot, \cdot)_\Omega$ the \mathcal{L}^2 inner product over the domain Ω , and defining $\dot{c} := \frac{\partial c}{\partial t}$ we have:

$$B(w; \dot{c}, c) := (w, \dot{c})_\Omega + (w, \mathbb{N}_2 \mathbb{P} e \mathbf{u} \cdot \nabla c)_\Omega + (\nabla w, \mathbb{N}_2 M_c \nabla \mu_c + \nabla M_c \Delta c)_\Omega + (\Delta w, M_c \Delta c)_\Omega. \quad (3.3)$$

We integrate equation (3.2) by parts repeatedly to obtain the following Euler-Lagrange form of the equation:

$$\left(w, \frac{\partial c}{\partial t} + \mathbb{N}_2 \mathbb{P} e \mathbf{u} \cdot \nabla c - \nabla \cdot (M_c \nabla (\mathbb{N}_2 \mu_c - \Delta c)) \right)_\Omega = 0, \quad (3.4)$$

which is consistent with the strong form (2.23).

3.2 The semi-discrete formulation

We spatially discretize the advective Cahn-Hilliard equation by using NURBS basis functions [41, 49]; see also section 4. Since it is possible to select NURBS basis functions of degree $p \geq 2$ which are globally \mathcal{C}^{p-1} -continuous, we are able to directly discretize the weak form (3.2) by means of the Galerkin method. Let $\mathcal{V}^h \subset \mathcal{V}$ denote the finite dimensional function space spanned by such NURBS basis functions in two or three-dimensions and satisfying the essential boundary conditions. We approximate equation (3.2) in space as follows:

$$\begin{aligned} \text{find } c^h(t) \in \mathcal{L}^2(0, T; \mathcal{V}^h) \cap \mathcal{H}^1(0, T; \mathcal{L}^2(\Omega)) : \\ B(w^h; \dot{c}^h(t), c^h(t)) = 0 \quad \forall w^h \in \mathcal{V}^h, \quad t \in [0, T), \\ \text{with } c^h(0) = c_0^h \quad \text{in } \Omega, \end{aligned} \quad (3.5)$$

where c_0^h is the \mathcal{L}^2 projection of the function c_0 onto \mathcal{V}^h . The weighting function w^h and trial solution c^h can be written as:

$$w^h = \sum_{A=1}^{n_{bf}} w_A R_A, \quad (3.6)$$

$$c^h = \sum_{A=1}^{n_{bf}} c_A R_A. \quad (3.7)$$

where the NURBS basis functions R_A define the discrete space \mathcal{V}^h of dimension n_{bf} and the coefficients c_A represent the control variables.

Remark 4. *It is well-known that the thickness of interfaces between the two phases in the Cahn-Hilliard equation is proportional to $\sqrt{\lambda}$. Hence, in order to accurately capture and represent these interfaces, the mesh size associated to the spatial approximation should be chosen sufficiently “small”. Numerical experiments carried out in [31, 43] indicate that the mesh size h should be chosen according to the following criterion:*

$$h \leq \sqrt{\frac{\lambda}{\tau}}, \quad (3.8)$$

with τ being a positive non-dimensional constant. According to our experience, violation of this criterion may result in severe overshoots and undershoots of the solution in proximity of the interfaces, which in turn lead to unphysical results. For all the physical conditions considered in this work, we have found the choice of $\tau = 2.5$ adequate for two-dimensional simulations, and the choice of $\tau = 1$ adequate for three-dimensional problems.

3.3 Time discretization

Several time discretization schemes have been utilized in the numerical solution of the Cahn-Hilliard equation, including the backward Euler method [50], the Crank-Nicolson method [58], and higher order implicit Runge-Kutta methods [59]. In this work, we use the generalized- α method [17, 44], a fully implicit time discretization scheme with controllable numerical dissipation. We couple the generalized- α method with an adaptive time step strategy [20, 31], which allows us to adjust the time step, by several orders of magnitude, while maintaining the accuracy of the solution. This is particularly important in Cahn-Hilliard flows, due to the intermittent nature of the phase transition and the different time scales involved, including those induced by the advection field.

3.3.1 Time-stepping scheme

Let us start by subdividing the time interval $[0, T)$ into a set of n_{ts} time intervals of size $\Delta t_n := t_{n+1} - t_n$ delimited by a discrete time vector $\{t_n\}_{n=0}^{n_{ts}}$. In addition, we denote by

$\mathbf{C}_n = \mathbf{C}(t_n) = \{c_A(t_n)\}_{A=1}^{n_{bf}}$ and $\dot{\mathbf{C}}_n = \dot{\mathbf{C}}(t_n) = \{\dot{c}_A(t_n)\}_{A=1}^{n_{bf}}$ the vectors of control variables and time derivatives evaluated at the time step t_n . We define the residual vector as:

$$\mathbf{Q}(\dot{\mathbf{C}}_n, \mathbf{C}_n) := \{Q_A(\mathbf{C}_n, \dot{\mathbf{C}}_n)\}, \quad (3.9)$$

$$Q_A(\dot{\mathbf{C}}_n, \mathbf{C}_n) := B(R_A; \dot{c}^h(t_n), c^h(t_n)). \quad (3.10)$$

Then, the generalized- α algorithm can be stated as follows: at the time step t_n , given $\dot{\mathbf{C}}_n$, \mathbf{C}_n , the time step $\Delta t_n = t_{n+1} - t_n$, and parameters α_m , α_f and δ :

$$\begin{aligned} \text{find } & \dot{\mathbf{C}}_{n+1}, \mathbf{C}_{n+1}, \dot{\mathbf{C}}_{n+\alpha_m}, \text{ and } \mathbf{C}_{n+\alpha_f} : \\ & \mathbf{Q}(\dot{\mathbf{C}}_{n+\alpha_m}, \mathbf{C}_{n+\alpha_f}) = 0, \\ & \mathbf{C}_{n+1} = \mathbf{C}_n + \Delta t_n \dot{\mathbf{C}}_n + \delta \Delta t_n (\dot{\mathbf{C}}_{n+1} - \dot{\mathbf{C}}_n), \\ & \dot{\mathbf{C}}_{n+\alpha_m} = \dot{\mathbf{C}}_n + \alpha_m (\dot{\mathbf{C}}_{n+1} - \dot{\mathbf{C}}_n), \\ & \mathbf{C}_{n+\alpha_f} = \mathbf{C}_n + \alpha_f (\mathbf{C}_{n+1} - \mathbf{C}_n). \end{aligned} \quad (3.11)$$

The parameters α_m , α_f and δ are chosen on the basis of accuracy and stability considerations. It has been shown in [44] that, for linear problems, an unconditionally stable, second-order accurate scheme is attained for:

$$\delta = \frac{1}{2} + \alpha_m - \alpha_f, \quad \alpha_m \geq \alpha_f \geq \frac{1}{2}. \quad (3.12)$$

The parameters α_m and α_f can be parametrized in terms of ρ_∞ , the limit of the spectral radius of the amplification matrix for $\Delta t \rightarrow \infty$, as:

$$\alpha_m = \frac{1}{2} \left(\frac{3 - \rho_\infty}{1 + \rho_\infty} \right), \quad \alpha_f = \frac{1}{1 + \rho_\infty}. \quad (3.13)$$

With the above parametrization and δ given in (3.12), a family of second-order accurate and unconditionally stable time integration schemes is defined in terms of the parameter $\rho_\infty \in [0, 1]$. It has been demonstrated that ρ_∞ controls the high-frequency dissipation [40, 44]. For linear problems, if ρ_∞ is chosen to be zero, the method annihilates the high numerical frequencies in one step, and if ρ_∞ is chosen to be one, the high frequencies are preserved. Generally, it is advisable to select ρ_∞ strictly less than one so that high frequencies do not spoil long time simulations. The choice of $\rho_\infty = 0.5$ has been shown to be effective for turbulence computations [5, 44] as well as for the Cahn-Hilliard equation [31], and we have adopted this value in all of our numerical simulations.

Remark 5. *A provably unconditionally stable-in-energy, second-order-accurate algorithm for the Cahn-Hilliard equation has recently been developed by Gómez and Hughes [32]. In numerical tests, we have found the generalized- α algorithm and the algorithm of [32] to behave similarly. However, the generalized- α algorithm has not been proved to be unconditionally stable in energy. This work was begun before work on the Gómez-Hughes algorithm*

was completed and therefore we continued with the generalized- α algorithm until this work was completed. We anticipate that there would have been no differences in our results or conclusions had the the Gómez-Hughes algorithm been used.

Remark 6. If we choose $\alpha_f = \alpha_m = \delta = 1$, the generalized- α method coincides with the backward Euler method [50], which is unconditionally stable but only first-order accurate.

We solve the nonlinear system of equations given in (3.11) by using the Newton method [50]. Specifically, the control variables \mathbf{C}_{n+1} at each time step t_{n+1} , with $n = 0, \dots, n_{ts} - 1$, is obtained iteratively by means of the following predictor-multicorrector scheme in the variables $\mathbf{C}_{n+1,(i)}$ for $i = 0, \dots, i_{max}$.

Predictor stage: Set:

$$\mathbf{C}_{n+1,(0)} = \mathbf{C}_n, \quad (3.14)$$

$$\dot{\mathbf{C}}_{n+1,(0)} = \frac{\delta - 1}{\delta} \dot{\mathbf{C}}_n. \quad (3.15)$$

$$(3.16)$$

Multicorrector stage: Repeat the following steps $i = 1, 2, \dots, i_{max}$:

1. Evaluate the control variables at the intermediate stage:

$$\dot{\mathbf{C}}_{n+\alpha_m,(i)} = \dot{\mathbf{C}}_n + \alpha_m (\dot{\mathbf{C}}_{n+1,(i-1)} - \dot{\mathbf{C}}_n), \quad (3.17)$$

$$\mathbf{C}_{n+\alpha_f,(i)} = \mathbf{C}_n + \alpha_f (\mathbf{C}_{n+1,(i-1)} - \mathbf{C}_n). \quad (3.18)$$

2. Assemble the residual vector of the nonlinear system using the above intermediate stage solution:

$$\mathbf{Q}_{(i)} := \mathbf{Q}(\dot{\mathbf{C}}_{n+\alpha_m,(i)}, \mathbf{C}_{n+\alpha_f,(i)}). \quad (3.19)$$

3. If the following criterion on the relative norm of the residual

$$\frac{\|\mathbf{Q}_{(i)}\|}{\|\mathbf{Q}_{(0)}\|} < tol_Q \quad (3.20)$$

is satisfied for a prescribed tolerance tol_Q , set the control variables at time step t_{n+1} as $\dot{\mathbf{C}}_{n+1} = \dot{\mathbf{C}}_{n+1,(i-1)}$ and $\mathbf{C}_{n+1} = \mathbf{C}_{n+1,(i-1)}$, and exit the multicorrector stage; otherwise, continue to step 4.

4. Assemble the tangent matrix of the nonlinear system and solve the linear system of equations:

$$\mathbf{K}_{(i)} := \alpha_m \frac{\partial \mathbf{Q}(\dot{\mathbf{C}}_{n+\alpha_m,(i)}, \mathbf{C}_{n+\alpha_f,(i)})}{\partial \dot{\mathbf{C}}_{n+\alpha_m,(i)}} + \alpha_f \delta \Delta t_n \frac{\partial \mathbf{Q}(\dot{\mathbf{C}}_{n+\alpha_m,(i)}, \mathbf{C}_{n+\alpha_f,(i)})}{\partial \mathbf{C}_{n+\alpha_f}}, \quad (3.21)$$

$$\mathbf{K}_{(i)} \Delta \dot{\mathbf{C}}_{n+1,(i)} = -\mathbf{Q}_{(i)}. \quad (3.22)$$

5. Use the solution $\Delta\dot{\mathbf{C}}_{n+1,(i)}$ to update the control variables as:

$$\dot{\mathbf{C}}_{n+1,(i)} = \dot{\mathbf{C}}_{n+1,(i-1)} + \Delta\dot{\mathbf{C}}_{n+1,(i)} \quad (3.23)$$

$$\mathbf{C}_{n+1,(i)} = \mathbf{C}_{n+1,(i-1)} + \delta\Delta t_n \Delta\dot{\mathbf{C}}_{n+1,(i)} \quad (3.24)$$

and return to step 1.

For our numerical simulations, we reduce the relative norm of the nonlinear residual to the tolerance $tol_Q = 10^{-4}$ for each time step (3.20). We use the GMRES method [51] to solve the linear system (3.22) with a stopping criterion based on the norm of the relative residuals and tolerance equal to 10^{-6} . We employ an algebraic multigrid preconditioner for the two-dimensional simulations and an incomplete-LU factorization for the three-dimensional simulations.

3.3.2 Time step adaptivity

We employ the same adaptive scheme proposed in [20, 31]. This scheme is based on the comparison of the solutions obtained with the generalized- α method and the backward Euler method in order to properly adjust the time step size. With this scheme, at each time step t_n , given $\dot{\mathbf{C}}_n$, \mathbf{C}_n and time step Δt_{n-1} , the following steps are repeated for $l = 1, \dots, l_{max}$, with $\Delta t_{n,(0)} = \Delta t_{n-1}$:

1. Compute the control variables $\mathbf{C}_{n+1,(l-1)}^{BE}$ using the backward Euler method and $\Delta t_{n,(l-1)}$.
2. Compute the control variables $\mathbf{C}_{n+1,(l-1)}^\alpha$ using the generalized- α method and $\Delta t_{n,(l-1)}$.
3. Calculate the relative error $e_{n+1,(l-1)} := \frac{\|\mathbf{C}_{n+1,(l-1)}^{BE} - \mathbf{C}_{n+1,(l-1)}^\alpha\|}{\|\mathbf{C}_{n+1,(l-1)}^\alpha\|}$.
4. Update the time step size according to the following formula

$$\Delta t_{n,(l)} = \varrho \left(\frac{TOL}{e_{n+1,(l-1)}} \right)^{1/2} \Delta t_{n,(l-1)} \quad (3.25)$$

with TOL a prescribed tolerance and ϱ a suitable safety coefficient.

5. If $e_{n+1,(l-1)} \geq TOL$, return to step 1; otherwise, set $\dot{\mathbf{C}}_{n+1} = \dot{\mathbf{C}}_{n+1,(l-1)}$, $\mathbf{C}_{n+1} = \mathbf{C}_{n+1,(l-1)}$, and $\Delta t_n = \Delta t_{n,(l)}$.

For our numerical simulations, we select $\varrho = 0.85$, and $TOL = 10^{-3}$. This adaptive strategy enables capturing the Cahn-Hilliard coarsening phenomena without resorting to a uniform and prohibitively small time step size. Consequently, we are able to reach a steady state solution for all the simulations considered in this work.

4 Essential boundary conditions with NURBS basis: periodic conditions and Bézier extraction operators

In this section, we construct the discrete space $\mathcal{V}^h \subset \mathcal{V}$ introduced in section 3.2 for the approximation of the function space \mathcal{V} (3.1). The space \mathcal{V}^h is obtained by the span of NURBS basis functions of degree $p \geq 2$ to achieve global C^1 continuity. In particular, we discuss the imposition of the essential no-flux boundary condition $\nabla c^h \cdot \mathbf{n} = 0$ on Γ_s and the periodic boundary conditions $c^h|_{\Gamma_{in}} = c^h|_{\Gamma_{out}}$ and $\nabla c^h \cdot \mathbf{n}|_{\Gamma_{in}} = -\nabla c^h \cdot \mathbf{n}|_{\Gamma_{out}}$ within the framework of Bézier extraction [8].

4.1 B-splines, NURBS, and Bézier extraction

We review the construction of B-splines and NURBS basis functions [18, 41, 49] and, in view of the use of Bézier extraction methods, we recall Bézier data structures including the extraction operators [8]. For the sake of simplicity, we consider the case of a curve in a d -dimensional space, with $d = 1, 2, 3$; the more general cases of multivariate NURBS surfaces and solids can be straightforwardly obtained by virtue of tensor product construction.

A univariate B-spline curve $T(\xi) : \widehat{\Omega} \rightarrow \Omega \subset \mathbb{R}^d$, for $d = 1, 2, 3$, is defined on a parametric space $\widehat{\Omega} := [\xi_1, \xi_{n+p+1})$ discretized by the knot vector $\Xi = \{\xi_i\}_{i=1}^{n+p+1}$, where p is the polynomial degree and n is the total number of basis functions,

$$T(\xi) := \sum_{A=1}^n \mathbf{P}_A N_{A,p}(\xi) = \mathbf{P}^T \mathbf{N}(\xi), \quad (4.1)$$

and $\mathbf{N}(\xi) := \{N_{A,p}(\xi)\}_{A=1}^n$ is the set of n B-spline basis functions and $\mathbf{P} := \{\mathbf{P}_A\}_{A=1}^n \in \mathbb{R}^{n \times d}$ is the set of control points. The basis functions $N_{A,p}(\xi)$, for $A = 1, \dots, n$ and $\xi \in \widehat{\Omega}$, are obtained by means of the recursive Cox-de Boor formula:

$$N_{A,0}(\xi) = \begin{cases} 1 & \xi_A \leq \xi < \xi_{A+1}, \\ 0 & \text{otherwise,} \end{cases} \quad (4.2)$$

$$N_{A,p}(\xi) = \frac{\xi - \xi_A}{\xi_{A+p} - \xi_A} N_{A,p-1}(\xi) + \frac{\xi_{A+p+1} - \xi}{\xi_{A+p+1} - \xi_{A+1}} N_{A+1,p-1}(\xi).$$

Similarly, a univariate NURBS curve is defined as:

$$T(\xi) := \sum_{A=1}^n \mathbf{P}_A R_{A,p}(\xi) = \mathbf{P}^T \mathbf{R}(\xi). \quad (4.3)$$

Here, $\mathbf{R}(\xi) := \{R_{A,p}(\xi)\}_{A=1}^n$ is the set of n NURBS basis functions obtained as:

$$\mathbf{R}(\xi) := \frac{1}{W(\xi)} \mathbf{W} \mathbf{N}(\xi), \quad (4.4)$$

where $\mathbf{W} := \text{diag}(\mathbf{w})$, $\mathbf{w} := \{w_A\}_{A=1}^n$, and the weight function $W(\xi) : \widehat{\Omega} \rightarrow \mathbb{R}$ is defined as:

$$W(\xi) := \sum_{B=1}^n w_B N_{B,p}(\xi) = \mathbf{w}^T \mathbf{N}(\xi). \quad (4.5)$$

The global smooth B-spline and NURBS curves (4.1) and (4.3) allow for a local representation in terms of C^0 -continuous Bézier (finite) elements $\mathbf{B}(\xi) := \{B_{A,p}(\xi)\}_{A=1}^{n+m}$, where m is the number of additional knots. The $p+1$ Bernstein polynomials with support in each knot span are obtained by an affine mapping from the corresponding reference Bernstein polynomials $\{B_{a,p}^{ref}(\eta)\}_{a=1}^{p+1}$ defined on $\eta \in [0, 1]$:

$$\begin{aligned} B_{a,0}^{ref}(\eta) &= 1, \\ B_{a,p}^{ref}(\eta) &= 0 \quad \text{if } a < 1 \text{ or } a > p+1, \\ B_{a,p}^{ref}(\eta) &= (1-\eta) B_{a,p-1}^{ref}(\eta) + \eta B_{a-1,p-1}^{ref}(\eta). \end{aligned} \quad (4.6)$$

The Bézier extraction operator $\mathbf{C} \in \mathbb{R}^{n \times (n+m)}$, is the linear operator which transforms the Bernstein polynomials $\mathbf{B}(\xi)$ to the B-spline basis functions $\mathbf{N}(\xi)$:

$$\mathbf{N}(\xi) = \mathbf{C} \mathbf{B}(\xi). \quad (4.7)$$

Similarly, following from (4.4), the NURBS basis could be written as:

$$\mathbf{R}(\xi) = \frac{1}{W(\xi)} \mathbf{W} \mathbf{C} \mathbf{B}(\xi), \quad (4.8)$$

while the weight function (4.5) reads:

$$W(\xi) = \mathbf{w}^T \mathbf{C} \mathbf{B}(\xi). \quad (4.9)$$

Further, if we introduce the weights associated with the Bézier basis functions $\mathbf{w}^b \in \mathbb{R}^{n+m}$:

$$\mathbf{w}^b := \mathbf{C}^T \mathbf{w}, \quad (4.10)$$

the diagonal matrix $\mathbf{W}^b := \text{diag}(\mathbf{w}^b)$, and the Bézier control points $\mathbf{P}^b \in \mathbb{R}^{(n+m) \times d}$:

$$\mathbf{P}^b := (\mathbf{W}^b)^{-1} \mathbf{C}^T \mathbf{W} \mathbf{P}. \quad (4.11)$$

then the Bézier representation of the NURBS curve (4.3) reads:

$$T(\xi) = \frac{1}{W^b(\xi)} (\mathbf{P}^b)^T \mathbf{W}^b \mathbf{B}(\xi). \quad (4.12)$$

As a final remark, we observe that the extraction operator \mathbf{C} is never computed explicitly, but rather its localized versions $\mathbf{C}_e \in \mathbb{R}^{(p+1) \times (p+1)}$ over the knot spans of Ξ are provided for the individual elements, $e = 1, \dots, n_{el}$.

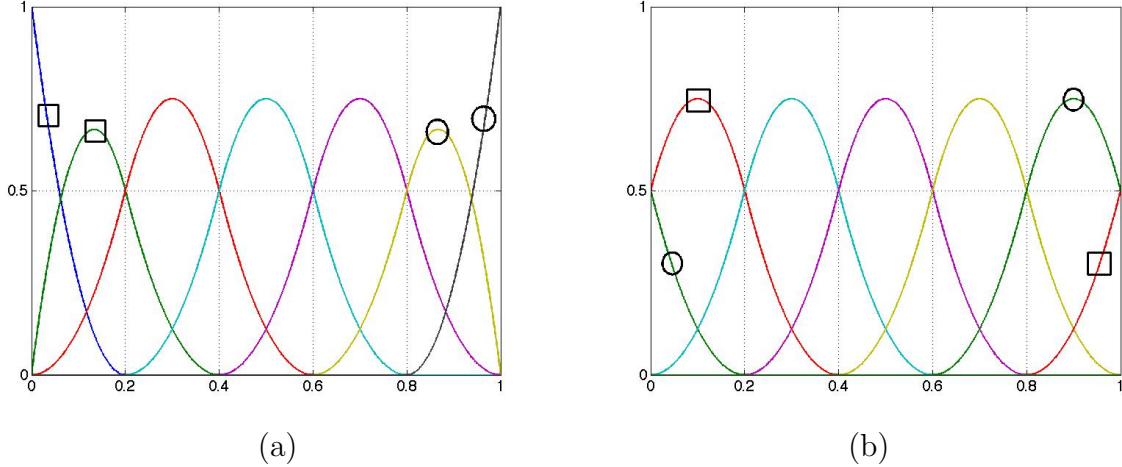


Figure 1: One-dimensional, quadratic, \mathcal{C}^1 -continuous B-spline basis with open knot vector $\Xi = \{\{0\}_{i=1}^3, 0.2, 0.4, 0.6, 0.8, \{1\}_{i=1}^3\}$ (a) and corresponding periodic B-spline basis (b). The circles and squares indicate the control variables which are set equal to enforce the no-flux condition (a) and periodic boundary conditions (b).

4.2 Strong imposition of essential boundary conditions

We discuss the strong imposition of the essential no-flux boundary condition $\nabla c^h \cdot \mathbf{n} = 0$ on Γ_s , as well as the periodic boundary conditions $c^h|_{\Gamma_{in}} = c^h|_{\Gamma_{out}}$ and $\nabla c^h \cdot \mathbf{n}|_{\Gamma_{in}} = -\nabla c^h \cdot \mathbf{n}|_{\Gamma_{out}}$. In particular, we highlight the modifications required on the Bézier data structures and on the global ID array [40]. In this section, we still limit our discussion to the case of partial differential equations defined on curves $T(\xi)$ in the d -dimensional space with $d = 1, 2, 3$.

It is convenient to express the approximate solution $c^h = c^h(\mathbf{x})$ defined on a curve $\mathbf{x}(\xi) = T(\xi)$ as the corresponding function $\hat{c}^h = \hat{c}^h(\xi)$ defined in terms of the parametric coordinate. $c^h(\mathbf{x})$ and $\hat{c}^h(\xi)$ has the following relations:

$$\hat{c}^h(\xi) = c^h(\mathbf{x}) \circ \mathbf{x}(\xi) \quad (4.13)$$

and,

$$\frac{d\hat{c}^h}{d\xi}(\xi) = (\nabla c^h(\mathbf{x}) \frac{d\mathbf{x}}{d\xi}) \circ \mathbf{x}(\xi). \quad (4.14)$$

4.2.1 No-flux essential condition

Following (4.14), the enforcement of the no-flux condition $\nabla c^h \cdot \mathbf{n} = 0$ is equivalent to imposing $\frac{d\hat{c}^h}{d\xi}(\xi_1) = \frac{d\hat{c}^h}{d\xi}(\xi_{n+p+1}) = 0$ along the parametric direction. Since we typically consider open-knot-vector B-splines and NURBS basis functions [49], such a boundary condition can

easily be satisfied by imposing the equality of the two consecutive control values of c^h at the boundary. Indeed, for a univariate, open-knot-vector NURBS basis, we have:

$$\begin{aligned}\frac{d\widehat{c}^h}{d\xi}(\xi_1) &= (c_2 - c_1) \frac{w_2}{w_1} \frac{dN_{2,p}}{d\xi}(\xi_1), \\ \frac{d\widehat{c}^h}{d\xi}(\xi_{n+p+1}) &= (c_{n-1} - c_n) \frac{w_{n-1}}{w_n} \frac{dN_{n-1,p}}{d\xi}(\xi_{n+p+1}).\end{aligned}\tag{4.15}$$

By setting the control variables $c_1 = c_2$ and $c_n = c_{n-1}$ we achieve the strong imposition of the essential no-flux conditions. In figure 1(a) we highlight this with an example of a B-spline basis.

From the implementation point of view, in an isogeometric analysis code, the enforcement of the no-flux boundary conditions only requires the modification of the global ID array without any change on the Bézier data structures. For the example of figure 1(a), the following ID array:

1	2	3	4	5	6	7
---	---	---	---	---	---	---

is modified to:

1	1	2	3	4	5	5
---	---	---	---	---	---	---

with the number of equations reduced from 7 to 5 for a scalar problem.

4.2.2 Periodic boundary conditions

As done before, we recast the imposition of the periodic boundary conditions $c^h|_{\Gamma_{in}} = c^h|_{\Gamma_{out}}$ and $\nabla c^h \cdot \mathbf{n}|_{\Gamma_{in}} = -\nabla c^h \cdot \mathbf{n}|_{\Gamma_{out}}$ to the case of a univariate NURBS curve. For a symmetric geometry with uniform parametrization, we have $\frac{d\mathbf{x}}{d\xi}(\xi_1) = \frac{d\mathbf{x}}{d\xi}(\xi_{n+p+1})$. Then following from (4.13) and (4.14), the periodic boundary conditions on the physical domain are equivalent to require periodic boundary conditions on the parametric domain:

$$\begin{aligned}\widehat{c}^h(\xi_1) &= \widehat{c}^h(\xi_{n+p+1}), \\ \frac{d\widehat{c}^h}{d\xi}(\xi_1) &= \frac{d\widehat{c}^h}{d\xi}(\xi_{n+p+1}).\end{aligned}\tag{4.16}$$

When we consider an open-knot-vector NURBS basis, the conditions (4.16) in combination with (4.15) lead to the following algebraic constraints among the control variables c_1 , c_2 , c_{n-1} , and c_n :

$$c_1 = c_n,\tag{4.17}$$

$$(c_2 - c_1) \frac{w_2}{w_1} \frac{dN_{2,p}}{d\xi}(\xi_1) = (c_{n-1} - c_n) \frac{w_{n-1}}{w_n} \frac{dN_{n-1,p}}{d\xi}(\xi_{n+p+1}).\tag{4.18}$$

From an implementation point of view, the above constraints do not require any modification of the Bézier data structures. However, while the constraint (4.17) can be easily enforced

by modifying the global ID array, the algebraic relation (4.18) needs to be explicitly taken into account when assembling the linear system (3.22). A modification of the assembling procedure is therefore required. To avoid such a modification, an alternative way is to employ periodic NURBS basis functions, which are defined as follows:

Definition 4.1. A globally C^q -continuous NURBS basis $\mathbf{R}^{per}(\xi) := \{R_{A,p}^{per}(\xi)\}_{A=1}^n$ of degree p , with $0 \leq q \leq p - 1$, is periodic if for any function $\widehat{c}^h(\xi) = \sum_{A=1}^n c_A^{per} R_{A,p}^{per}(\xi)$ in its span, the periodic boundary conditions:

$$\frac{d^k \widehat{c}^h}{d\xi^k}(\xi_1) = \frac{d^k \widehat{c}^h}{d\xi^k}(\xi_{n+p+1}) \quad \text{for } k = 0, \dots, q, \quad (4.19)$$

are satisfied by setting $c_A^{per} = c_{n-(q+1)+A}^{per}$ for $A = 1, \dots, q + 1$.

We notice that the standard concept of a periodic basis as a set of basis functions obtained by recursively replicating a reference basis function only holds if we consider B-splines with a uniform knot distribution. Indeed, in the case of NURBS, the presence of the weights does not allow for the use of such an intuitive definition. Finally, we observe that in the isogeometric context, the geometric map $\mathbf{x} = T(\xi)$ must also be equivalently represented in terms of the periodic basis. This goal is achieved by updating the control points for periodic basis functions. The details of this updating procedure are described in appendix A.

The use of a periodic NURBS basis allows us to enforce the periodic boundary conditions simply by modifying the global ID array. In the next section, we investigate how to obtain the periodic Bézier data structures starting from an existing open-knot-vector representation of a NURBS basis. If we refer to the example reported in figure 1(b), we have that the periodic boundary conditions for this globally C^1 -continuous periodic B-spline basis of degree 2 are enforced by modifying the ID array:

1	2	3	4	5	6	7
---	---	---	---	---	---	---

as:

1	2	3	4	5	1	2
---	---	---	---	---	---	---

for which the number of equations reduces from 7 to 5 for a scalar problem.

4.3 Periodic Bézier extraction operator

In this section we discuss the definition of a periodic NURBS basis for the imposition of the periodic boundary conditions according to Definition 4.1. In particular, we discuss the representation of the periodic NURBS basis in terms of the Bézier extraction data structures. For more details we refer the reader to appendices A-C.

We introduce a periodic transformation operator $\mathbf{T}^{per} \in \mathbb{R}^{n \times n}$, such that the periodic NURBS basis $\mathbf{R}^{per}(\xi) \in \mathbb{R}^n$ is obtained by linear transformation:

$$\mathbf{R}^{per}(\xi) = \mathbf{T}^{per} \mathbf{R}(\xi), \quad (4.20)$$

where $\mathbf{R}(\xi) \in \mathbb{R}^n$ is the NURBS basis function defined from the knot vector Ξ . The periodic transformation operator \mathbf{T}^{per} is an invertible linear operator that preserves the partition-of-unity property. By using equation (4.8) and following the content of section 4.1 and appendix A, we may rewrite the periodic NURBS basis in terms of the Bernstein polynomials $\mathbf{B}(\xi)$ and the periodic Bézier extraction operator, $\mathbf{C}^{per} \in \mathbb{R}^{n \times (n+m)}$, i.e.:

$$\mathbf{R}^{per}(\xi) = \frac{1}{W(\xi)} \mathbf{W} \mathbf{C}^{per} \mathbf{B}(\xi). \quad (4.21)$$

The definition of the periodic Bézier extraction operator \mathbf{C}^{per} follows from (A.4) and (A.10):

$$\mathbf{C}^{per} := \mathbf{T}_{\mathbf{W}}^{per} \mathbf{C}, \quad (4.22)$$

where \mathbf{C} is the Bézier extraction operator associated to the NURBS basis $\mathbf{R}(\xi)$, and the weighted periodic transformation operator $\mathbf{T}_{\mathbf{W}}^{per}$ is defined as:

$$\mathbf{T}_{\mathbf{W}}^{per} := \mathbf{W}^{-1} \mathbf{T}^{per} \mathbf{W}. \quad (4.23)$$

As shown above, the periodic transformation operator is the object required. In appendix B, we show that under suitable hypotheses the periodic transformation operator for a NURBS basis is identical to the one used for the definition of a periodic B-spline basis. In other words, under the hypotheses, the transformation operator does not vary due to weights. Therefore, we may obtain \mathbf{T}^{per} by focusing on the B-spline basis. In appendix C, we show that the periodic transformation operator admits a localized representation over the knot spans and we provide ways to compute it. Once such localized periodic transformation operators $\mathbf{T}_e^{per} \in \mathbb{R}^{(p+1) \times (p+1)}$ are computed, we can evaluate the localized periodic Bézier extraction operators $\mathbf{C}_e^{per} \in \mathbb{R}^{(p+1) \times (p+1)}$ by

$$\mathbf{C}_e^{per} := \mathbf{T}_{\mathbf{W},e}^{per} \mathbf{C}_e, \quad (4.24)$$

Here $\mathbf{T}_{\mathbf{W},e}^{per} \in \mathbb{R}^{(p+1) \times (p+1)}$ is the localized weighted periodic transformation operator and is defined by:

$$\mathbf{T}_{\mathbf{W},e}^{per} := (\mathbf{W}_e)^{-1} \mathbf{T}_e^{per} \mathbf{W}_e, \quad (4.25)$$

where $\mathbf{W}_e := \text{diag}(\mathbf{w}_e)$ is the diagonal matrix with the local weights.

In appendix C, we also provide the explicit form of the localized Bézier extraction operators for univariate NURBS bases of degrees $p = 1, 2, 3$ under the hypotheses of appendix B. For example, for a univariate C^1 -continuous periodic NURBS basis of degree $p = 2$, the

localized periodic Bézier extraction operators $\mathbf{C}_e^{per} \in \mathbb{R}^{3 \times 3}$ read:

$$\mathbf{C}_e^{per} = \begin{cases} \begin{bmatrix} 1/2 & 0 & 0 \\ w_1/(2w_2) & 1 & 1/2 \\ 0 & 0 & 1/2 \end{bmatrix} & \text{for } e = 1, \\ \mathbf{C}_e & \text{for } e = 2, \dots, n_{el} - 1, \\ \begin{bmatrix} 1/2 & 0 & 0 \\ 1/2 & 1 & w_1/(2w_2) \\ 0 & 0 & 1/2 \end{bmatrix} & \text{for } e = n_{el}, \end{cases} \quad (4.26)$$

where we notice the presence of the weights in the operators in the knot spans $e = 1$ and $e = n_{el}$, with n_{el} the number of knot spans. The operators \mathbf{C}_e^{per} for the multivariate NURBS basis can be obtained by virtue of the tensor product rule. As a final remark, we observe that the strong imposition of the periodic boundary conditions on $c^h(\mathbf{x})$ follows by modifying the global ID array according to the Definition 4.1.

5 Numerical results

In this section, we numerically investigate the spinodal decomposition under shear flow using the methodology outlined in the preceding sections. The efficiency, accuracy, and robustness of the numerical approach has allowed us to achieve the following results:

- Phase transition and coarsening of the concentration up to the steady state solution. Although several simulations of shear-driven spinodal decomposition have been conducted [9, 16, 37, 48, 55, 57], steady state solutions have been obtained only in a few two-dimensional cases [37, 55] and, until now, never in the three-dimensional setting. In this work, we obtain steady state solutions for both the two-dimensional case in the square domain and in the Taylor-Couette cell, as well as in the three-dimensions in a cube.
- Study of the influence of the Péclet number on the morphology of the steady state. As mentioned previously, the steady state of shear-driven spinodal decomposition is characterized by bands stretched along the flow direction. It has been reported in [35] that the average diameter of the bands decreases for an increasing Péclet number. In particular, the authors observed extremely thin band structure for high Péclet number flows. As the Péclet number is increased even further, the average diameter of band structures approaches the interface thickness. This phenomenon has also been reported in [30, 35], and is referred to as “shear-induced homogenization”. In [22] the authors provided a power law, deduced from physical experiments, which relates the average band width to shear rate. We simulate the advective Cahn-Hilliard problem up to the steady state in the square domain for the range of Péclet numbers from 0.01 to 100.0, and we compare these results with the power laws obtained in [22, 35].

- Study of the dependence of solution morphology on the surface tension. The surface tension induces a coarsening mechanism and counterbalances the break-up effect enforced by the shear flow; as a consequence, a large surface tension generally leads to steady state morphologies possessing a small number of bands with large interfaces. We compare the steady state solutions obtained for different values of surface tension in the square domain.

Unless otherwise specified, for all the numerical simulations, the initial condition $c_0 = c_0(\mathbf{x})$ is chosen as:

$$c_0 = \bar{c} + \delta_c, \quad (5.1)$$

where $\bar{c} \in (0, 1)$ is a constant representing volume fraction and $\delta_c = \delta_c(\mathbf{x}) : \Omega \rightarrow \mathbb{R}$ is a random function with uniform distribution such that $\delta_c(\mathbf{x}) \in [-0.05, 0.05]^1$. For the dimensional analysis of the problem, the dimensionless characteristic length and mobility variables in (2.17) are taken as $L_0 = 1$ and $M_0 = 1$.

The spatial discretization is comprised of quadratic NURBS functions. For the numerical integration, we use a 3-point Gauss quadrature rule in each spatial direction which we have found to be accurate, stable, and reasonably efficient in our case. In this work, for two-dimensional simulations, we utilize meshes with 512^2 elements, and, for three-dimensional simulations, we utilize meshes with 80^3 elements. For the time integration, we assume a final simulation time of $T = 10^4$ in order to achieve steady state solutions without prematurely interrupting the numerical simulations. The initial time step for all simulations is set to $\Delta t_0 = 10^{-12}$.

5.1 Two-dimensional results in a square domain

We start by considering the shear-driven spinodal decomposition in the square domain $\Omega = (0, 1)^2$ depicted in figure 2. The divergence-free advection field \mathbf{u} with shear rate γ is:

$$\mathbf{u} = \gamma y \hat{\mathbf{x}}. \quad (5.2)$$

The left boundary of the square coincides with the inflow boundary Γ_{in} while the right boundary Γ_{out} with the outflow boundary. We impose periodic boundary conditions at these inflow/outflow boundaries. The top and bottom boundaries of the square, which we identify with Γ_s , are modeled as solid walls, where the no-flux boundary condition is imposed. We assume the volume fraction is $\bar{c} = 0.5$ and, unless otherwise specified, we set the surface tension parameter to $\lambda = 9.54 \cdot 10^{-6}$. We observe that the condition (3.8) is satisfied for $\tau = 2.5$ and the mesh size $h = 1/256$. With this choice of surface tension, the dimensionless parameter \mathbb{N}_2 is equal to $1.05 \cdot 10^5$ and the characteristic time scale $T_0 = 1.05 \cdot 10^5$.

¹We require that $c_0 \in (0, 1)$ for all $\mathbf{x} \in \Omega$.

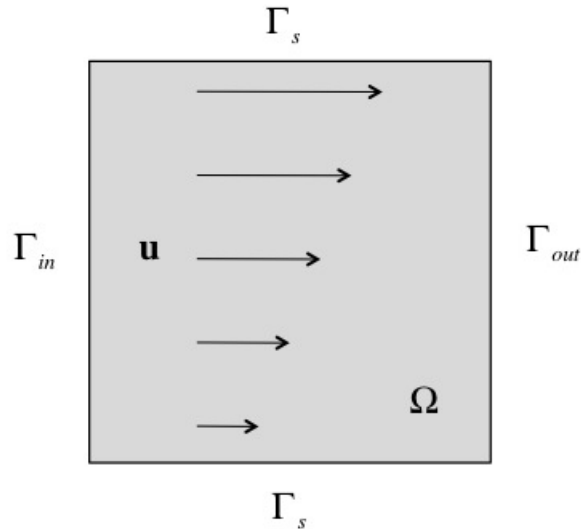


Figure 2: Problem setup for the square domain $\Omega = (0, 1)^2$.

5.1.1 Spinodal decomposition: phase transition to the steady state

We consider the phase transition up to steady state for two different values of the shear rate.

- (a) Figure 3 depicts the phase transition for $\mathbb{P}e = 1$. We observe that, in the early stages, evolution of the solution is driven primarily by the minimization of the chemical free energy. However, after approximately the time $t = 10^{-5}$, the coarsening due to the shear flow starts to play a dominant role, and a banded pattern aligned with the flow direction begins to form. At the steady state, we observe 6 bands.
- (b) Figure 4 depicts the phase transition for $\mathbb{P}e = 10$. We observe that phase separation due to minimization of the chemical free energy dominates the evolution until approximately $t = 10^{-6}$; after that the coarsening due to shear flow starts to play a dominant role in the formation of the banded pattern. At the steady state, we observe in this case 13 bands.

5.1.2 Dependence of the morphology of the steady state on Péclet number

In figure 5, we plot the steady state solutions obtained for the Péclet numbers $\mathbb{P}e = 0.01, 0.1, 1, 5, 10, 100$. We observe that, as expected, the width of the bands progressively decreases when increasing shear rate. The average band width w is computed as $w = L_0/N_{bands}$,

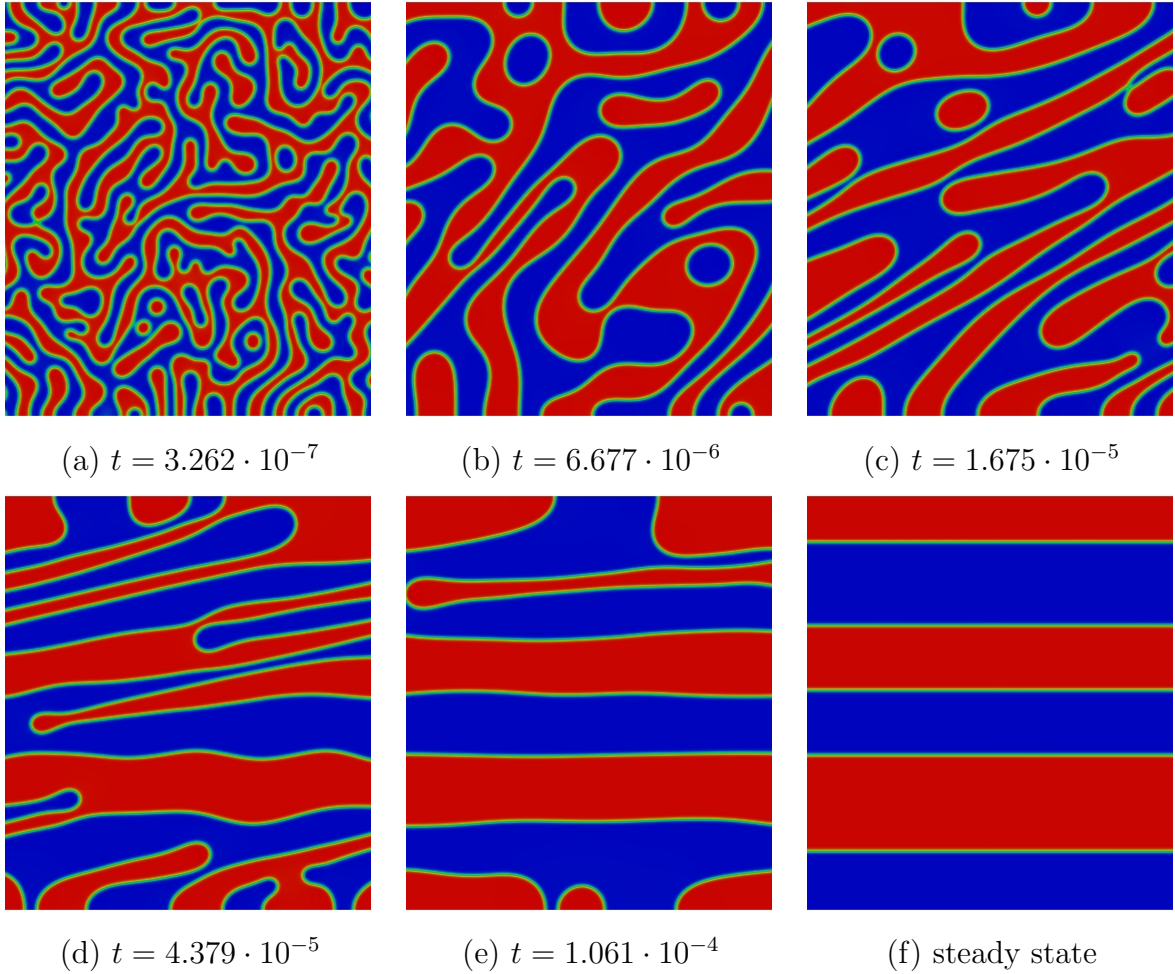


Figure 3: Phase transition in the square domain from a randomly perturbed initial solution to the steady state for $\mathbb{P}e = 1$.

where $N_{bands} = 2, 3, 6, 9, 13, 20$ for $\mathbb{P}e = 0.01, 0.1, 1, 5, 10, 100$, respectively. The relation between the average band width w and the shear rate γ is considered to obey a power relation of the form

$$w = C\gamma^{-\alpha} \quad (5.3)$$

for some shear-independent constant C . In [35], Hashimoto et al. analytically determined the range $[0.25, 0.33]$ for the values of α , while in [22], Derk et al. experimentally derived a value of $\alpha = 0.35$ for the spinodal decomposition of polymer mixtures under shear flow. In figure 6, we plot the average band width w as a function of γ as obtained for our numerical results and, for comparison, the power laws provided in [22] and [35]. By employing a least square fitting technique, we find that our numerical results obey the following power law:

$$w \sim \gamma^{-\alpha_{LS}} \quad \text{with } \alpha_{LS} = 0.259, \quad (5.4)$$

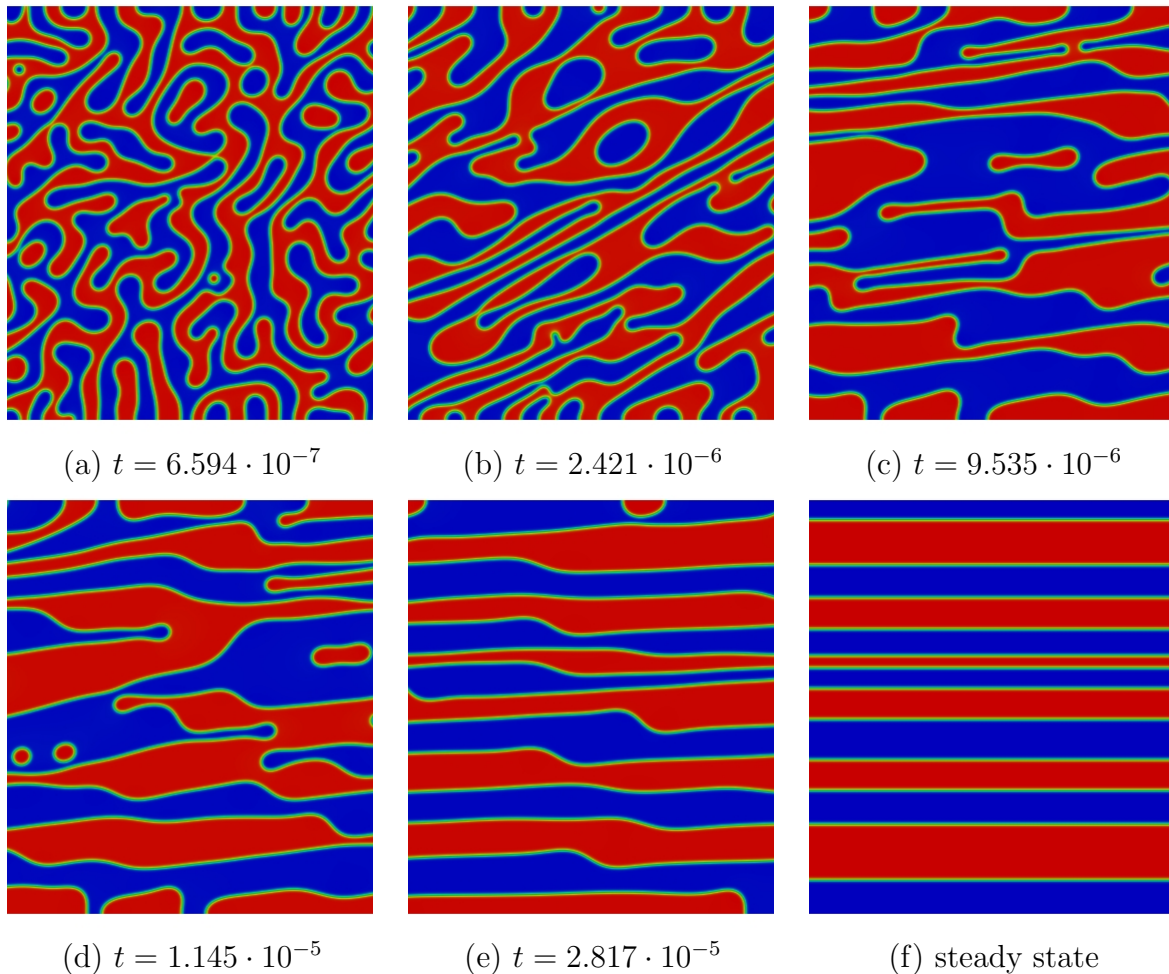


Figure 4: Phase transition in the square domain from a randomly perturbed initial solution to steady state for $\mathbb{P}e = 10$.

for which α_{LS} lays in the range predicted in [35]. However, we observe that this power law exhibits a lower exponent than the one experimentally derived by Derk et al. [22]; this being said, it has been reported that active Cahn-Hilliard fluids tend to exhibit higher numbers of banded structures than in the case of passive fluids [34].

5.1.3 Dependence of the morphology of the steady state on the surface tension parameter

In figure 8, we plot the steady state solutions obtained for $\mathbb{P}e = 1, 10$ with the surface tension parameter $\lambda = 6.10 \cdot 10^{-4}, 9.54 \cdot 10^{-6}$. We notice that for the larger surface tension parameter, only 2 bands are obtained for both $\mathbb{P}e = 1$ and $\mathbb{P}e = 10$. Furthermore, the thickness of the interfaces is considerably larger for $\lambda_{large} = 6.10 \cdot 10^{-4}$ than for $\lambda_{small} = 9.54 \cdot 10^{-6}$.

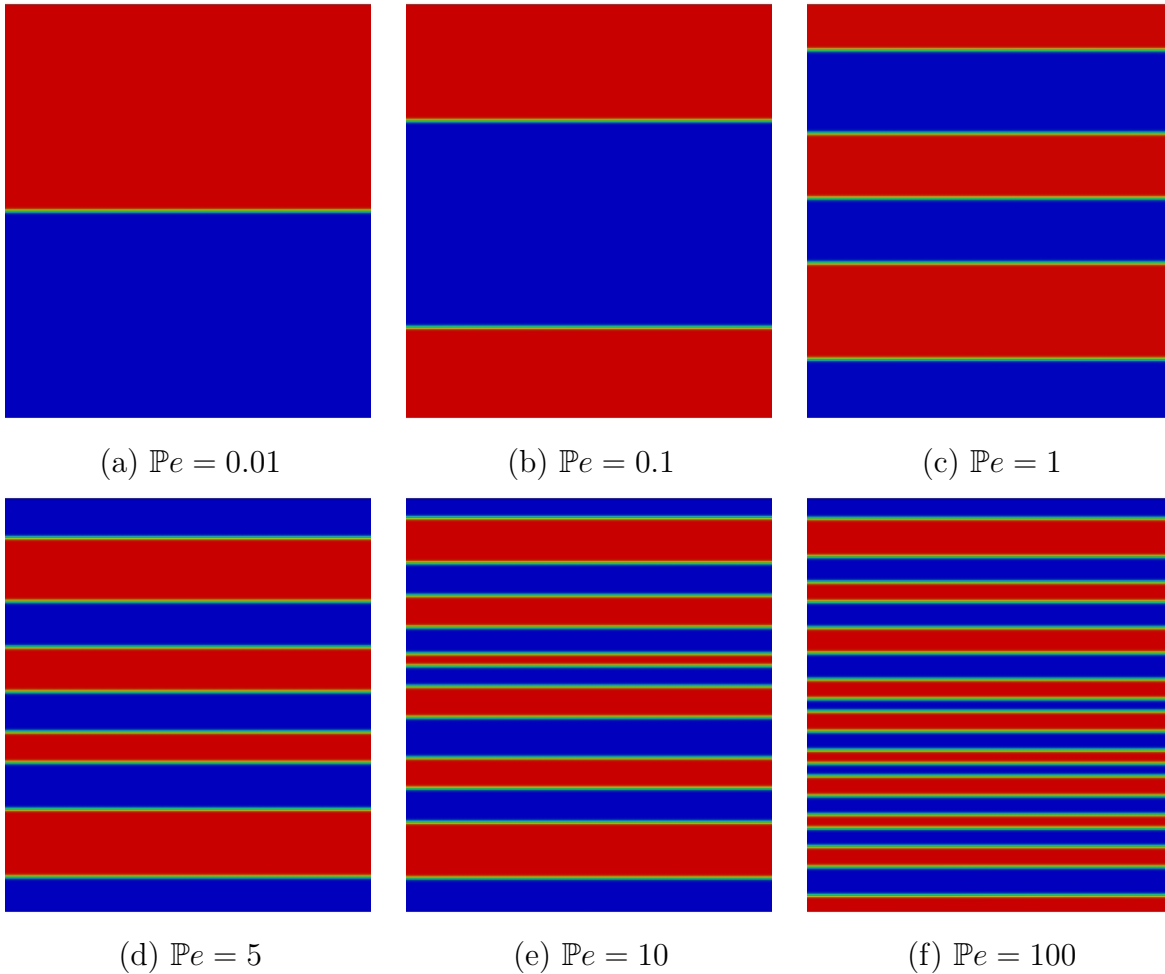


Figure 5: Steady state solutions for different values of the Péclet number.

Intermediate numbers of bands are obtained for values of λ within the range $(\lambda_{small}, \lambda_{large})$.

5.1.4 Numerical aspects

The use of the adaptive time step scheme of section 3.3.2 is crucial for the accuracy of the phase transition up to the steady state. In figure 7, we plot the evolution of the time step size Δt_n versus the time step t_n for three different values of the Péclet numbers, $\mathbb{P}e = 0.1, 1, 10$. We notice that the time step size experiences enormous changes in magnitude over the course of simulation time. Typically, the time step size grows with the time. However, the time step size also exhibits local reductions which correspond to nucleation mechanisms. As reported in figure 7(d), for high Péclet numbers, the time step size is generally smaller within the time range $t \in [10^{-7}, 10^{-4}]$ as the advective time scale imposes more stringent restrictions on Δt than coarsening phenomena typical of the Cahn-Hilliard equation. As a consequence,

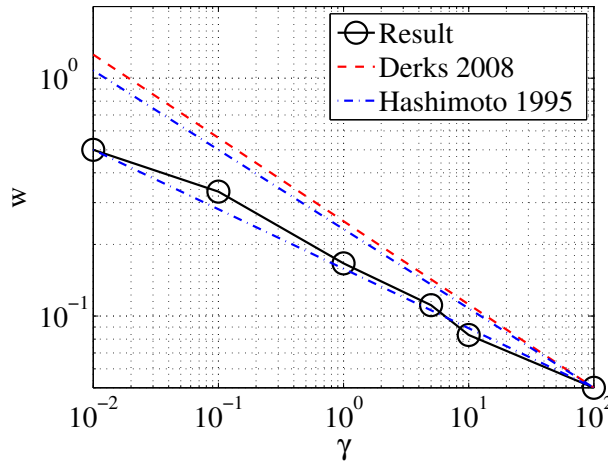


Figure 6: Log-log plot of the average band width w versus the shear rate γ as obtained by the numerical results of figure 5. The theoretical rates of Hashimoto et al. [35] and the experimental rate of Derk et al. [22] are also reported for comparison.

the total number of time steps required to reach the steady state increases with the Péclet number. In particular, our methodology requires 4,339, 10,589, 20,051 and 65,404 time steps for $\mathbb{P}e = 0.01, 0.1, 1.0,$ and $10.0,$ respectively.

Additionally, the number of Newton steps required for the convergence of our predictor-multicorrector scheme generally increases with the Péclet number, with 2 iterations typically being required for $\mathbb{P}e = 0.01$ and 5 for $\mathbb{P}e = 100$. Conversely, the number of GMRES iterations required for the solution of the linear system (3.22) decreases with the Péclet number. Typically, 250 GMRES iterations are required for $\mathbb{P}e = 0.01$ while only 40 iterations are required for $\mathbb{P}e = 100$.

In order to establish mesh independence for our methodology, we solved the advective Cahn-Hilliard problem on meshes comprised of $64^2, 128^2, 256^2$ and 512^2 elements for the case in which the surface tension parameter λ is equal to $\lambda_{large} = 6.10 \cdot 10^{-4}$ (note that the mesh size criterion (3.8) is satisfied for all these meshes for $\tau = 2.5$). The steady state solutions obtained for all these cases with the Péclet numbers $\mathbb{P}e = 1$ and $\mathbb{P}e = 10$ exhibit the same two banded morphology as depicted in figure 8(a) and (c). We also performed simulations with coarser meshes and we found convergence issues in the numerical method, accompanied by overshoots and undershoots of the concentration near the interfaces.

Finally, we notice that for a divergence-free advection field \mathbf{u} our numerical formulation conserves mass as expected for the advective Cahn-Hilliard equation. We typically obtain a negligible relative error on the mass, always less than $10^{-6}\%$ for the entire time range. The violation of conservation would ultimately lead to unphysical solution patterns; indeed, artificial mass sinks and sources, even of small magnitude, can lead to steady state solutions with incorrect patterns.

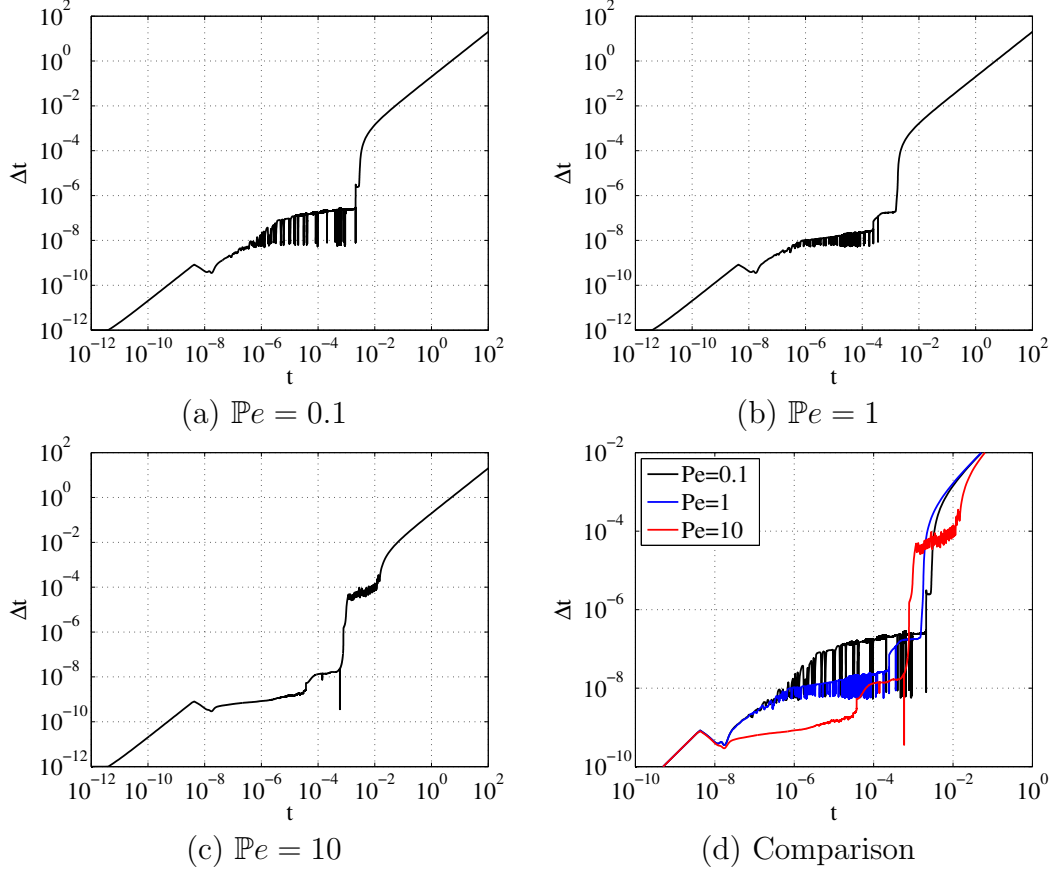


Figure 7: Evolution of the time step size Δt versus time t for $Pe = 0.1, 1, 10$.

5.2 Two-dimensional results for the Taylor-Couette cell

We consider the shear-driven spinodal decomposition occurring in the Taylor-Couette cell, for which an incompressible fluid is trapped between two concentric cylinders. We assume that the inner cylinder is rotating and the outer cylinder is fixed such that a Taylor-Couette flow is induced. The generated shear flow is depicted in figure 9. By denoting the radius of the inner cylinder as R_{in} and the outer cylinder as R_{out} , the advection field assumes the form:

$$\mathbf{u} = \mathbf{u}(r) = \gamma r \frac{\left(\frac{R_{in}}{r}\right)^2 - \eta^2}{1 - \eta^2} \hat{\boldsymbol{\theta}}, \quad (5.5)$$

where r is the distance from the origin, γ is the angular velocity of the inner cylinder, $\hat{\boldsymbol{\theta}}$ is a unit vector aligned with the direction of the shear flow, and $\eta := \frac{R_{in}}{R_{out}}$ is the radius ratio.

Note that $\mathbf{u}(R_{in}) = \gamma R_{in} \hat{\boldsymbol{\theta}}$ and $\mathbf{u}(R_{out}) = \mathbf{0}$.

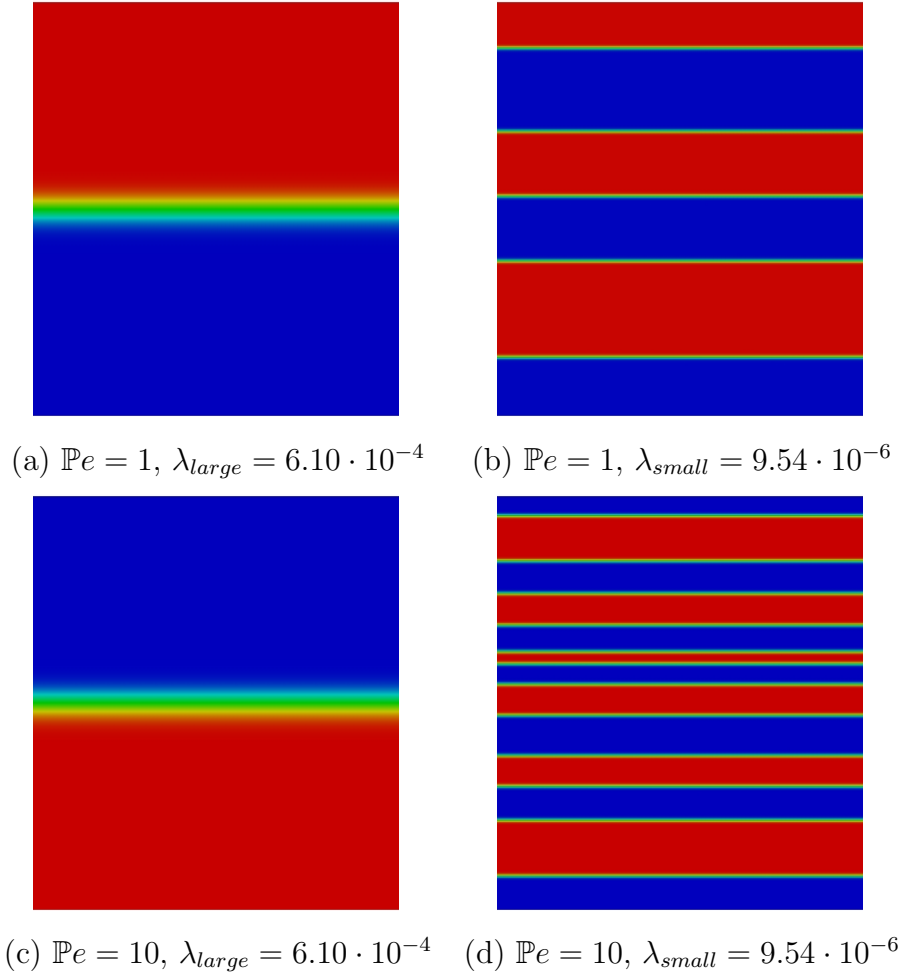


Figure 8: Steady state solutions for Péclet numbers and surface tension parameters.

For the parametrization of the Taylor-Couette cell by NURBS, we employ the hexagon-based NURBS construction of degree 2 outlined in [7], which ensures the basis is globally C^1 -continuous. For the numerical simulations, we solve the advective Cahn-Hilliard equation in a restricted domain representing 1/6 of the full Taylor-Couette cell as illustrated in figure 9. Periodic boundary conditions are imposed at the inflow/outflow boundary Γ_{in}/Γ_{out} to represent the Cahn-Hilliard flow in the whole Taylor-Couette cell. The circular boundaries Γ_s are modeled as solid walls.

Specifically, for the numerical simulations, we take $R_{in} = L_0$, $R_{out} = 2L_0$, $\bar{c} = 0.5$, and $\lambda = 9.54 \cdot 10^{-6}$. With these choices, we have $\mathbb{N}_2 = 1.05 \cdot 10^5$ and $T_0 = 1.05 \cdot 10^5$.

Figures 10 and 11 depict the phase transition in the Taylor-Couette cell for the Péclet numbers $\mathbb{P}e = 1$ and $\mathbb{P}e = 10$, respectively. For most of the phase transition, we observe similar phenomena to ones seen in the square domain case. That is, phase separation is initially dominated by the minimization of the chemical free energy, and coarsening due to

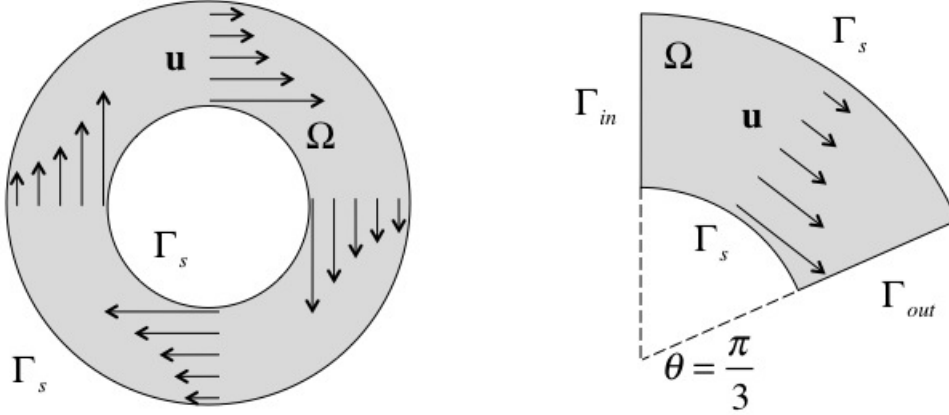


Figure 9: Taylor-Couette cell, ring computational domain, boundaries and shear flow \mathbf{u} .

shear flow plays a dominant role at latter times. The solution eventually evolves toward a banded structure where each band is fully aligned along the flow direction. As expected, the number of observed bands is larger for $\mathbb{P}e = 10$ than for $\mathbb{P}e = 1$, as in the square domain setting. However, as time evolves further towards the steady state, the bands located near the inner cylinder slowly disappear until there are only two bands remaining. We find that this process occurs regardless of Péclet number.

We notice that this is not entirely unexpected. In fact, once the solution evolves toward a banded structure where each band is aligned along the flow direction, we have $\nabla c \cdot \mathbf{u} = 0$ in Ω . Hence, the advective Cahn-Hilliard equation reduces to the standard Cahn-Hilliard equation, and the coarsening due to shear flow no longer plays a role in the evolution of the solution morphology. Instead, there only exists a competition between phase interfaces in order to reduce the surface free energy. In the square domain setting, at this stage, each interface has equivalent free energy as they all have the same length. Hence, the Cahn-Hilliard solution is at steady state, albeit a delicate one. However, in the Taylor-Couette cells, interfaces near the outer cylinder wall harbor more free energy than interfaces near the inner cylinder wall due to increased circumference. Thus, the Cahn-Hilliard equation is not at steady state, and the solution evolves to the two-banded structure.

In order to validate the instability of the intermediate, axisymmetric, banded solutions obtained in our simulations, we can perform an eigenvalue analysis. In particular, it is proven in [10] that c is a steady state of the Cahn-Hilliard equation if and only if all of the eigenvalues ω of the following linearized Cahn-Hilliard equation are non-positive:

$$\nabla \cdot \left[M_c \left(\frac{d\mu_c}{dc} \nabla v - \lambda \nabla(\Delta v) \right) \right] + \nabla(\mu_c - \lambda \Delta c) \cdot \left(\frac{dM_c}{dc} \nabla v \right) - \mathbf{u} \cdot \nabla v = \omega v. \quad (5.6)$$

As we are interested in evaluating the stability properties of intermediate axisymmetric solutions, we recast the above eigenvalue problem in terms of a single radial coordinate.

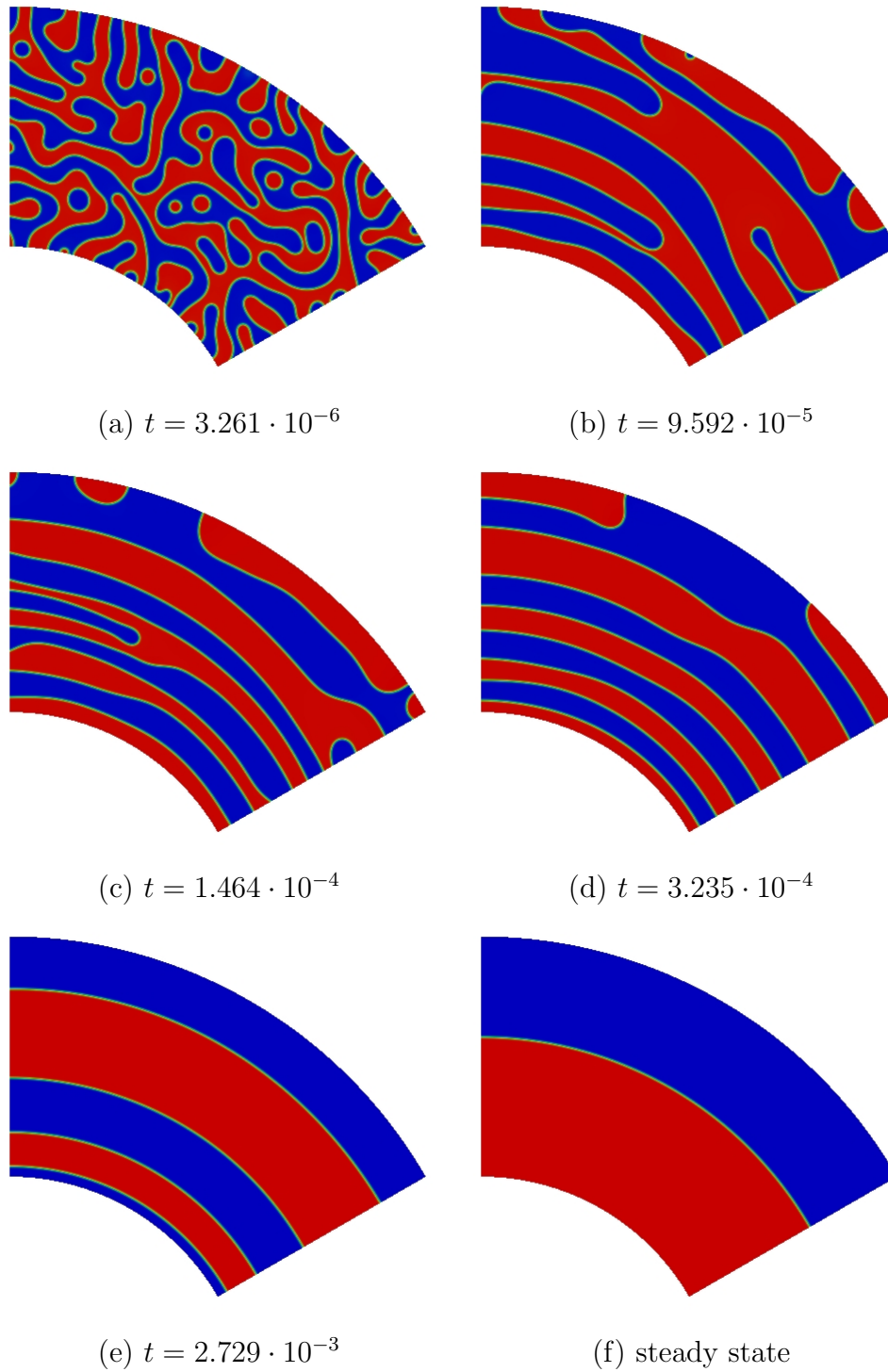
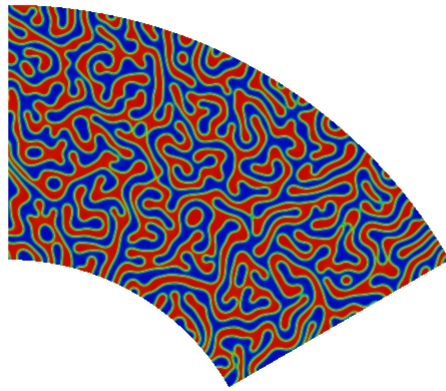
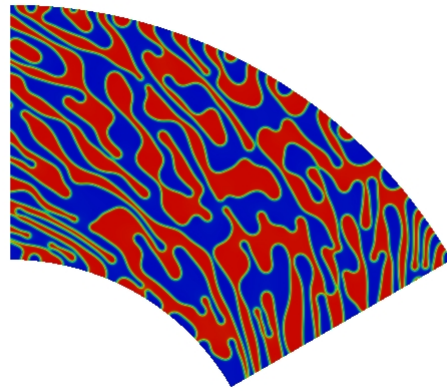
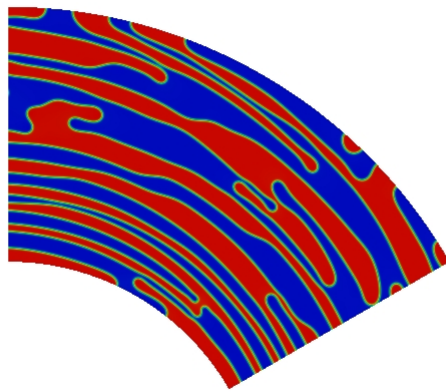
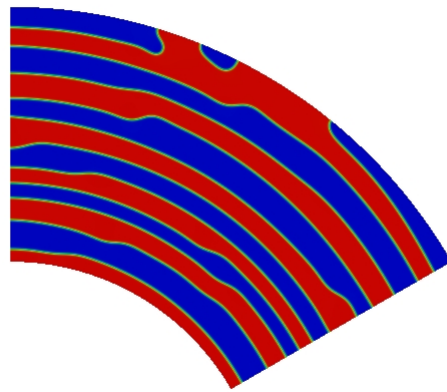
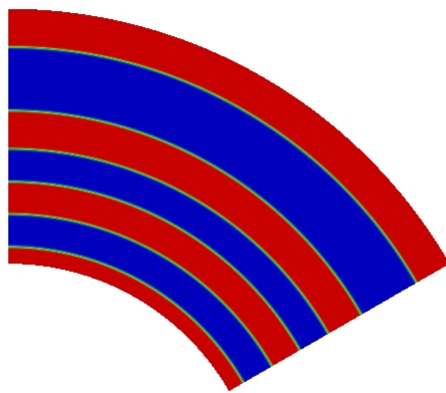
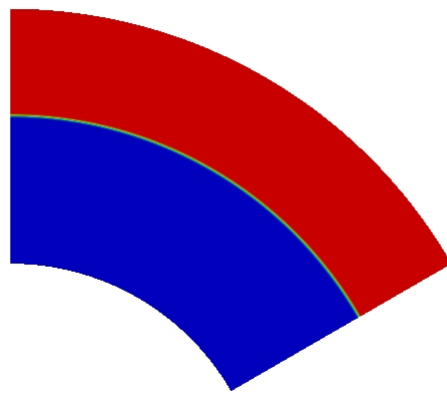


Figure 10: Phase transition in the Taylor-Couette cell for $\mathbb{P}e = 1$.

(a) $t = 3.038 \cdot 10^{-7}$ (b) $t = 2.223 \cdot 10^{-6}$ (c) $t = 1.762 \cdot 10^{-5}$ (d) $t = 5.303 \cdot 10^{-5}$ (e) $t = 1.675 \cdot 10^{-3}$ 

(f) steady state

Figure 11: Phase transition in the Taylor-Couette cell for $\mathbb{P}e = 10$.

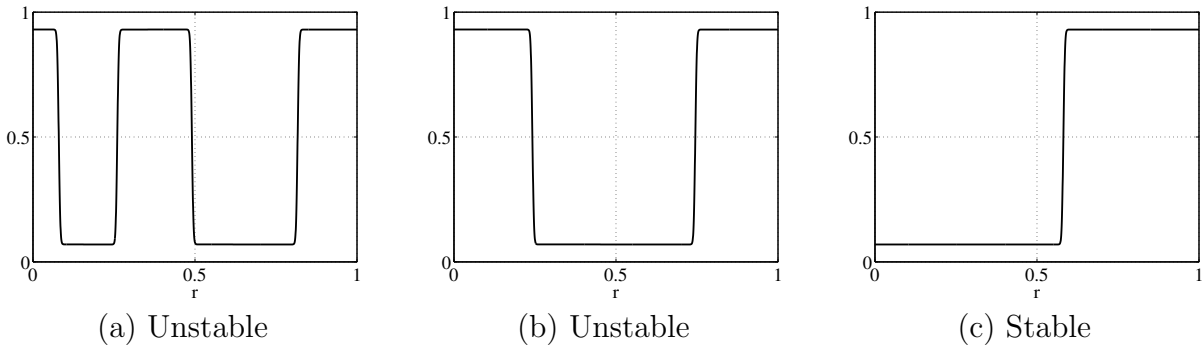


Figure 12: Unstable (a), (b) and stable (c) phase field solutions for the one-dimensional Cahn-Hilliard problem. Axisymmetric case; r is the radius.

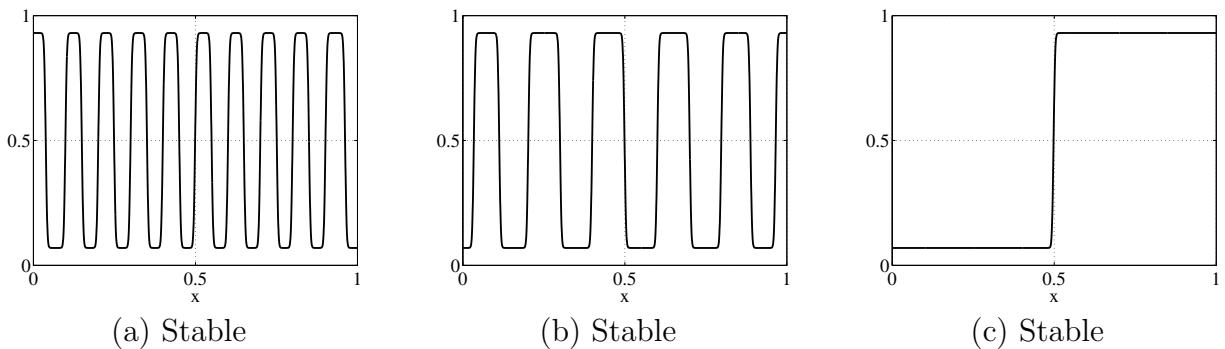


Figure 13: Stable phase field solutions for the one-dimensional Cahn-Hilliard problem. Rectilinear case; x is the Cartesian coordinate.

In figure 12, we plot three prototypical banded Cahn-Hilliard solutions in terms of the radial coordinate. The eigenvalue problems associated with the Cahn-Hilliard solutions in figure 12(a) and (b) were found to have positive eigenvalues, revealing their unstable nature. On the other hand, the eigenvalue problem associated with the solution in figure 12(c) was found to have only non-positive eigenvalues. Hence, it is a steady state solution of the axisymmetric Cahn-Hilliard equation. For reference, we report in figure 13 examples of stable steady state solutions obtained for the unit square, parametrized by x in order to reduce the problem to one spatial dimension. For all three of these solutions, the eigenvalue problem (5.6) was found to have no positive eigenvalues.

Remark 7. *In our experience, the exact satisfaction of periodic boundary conditions in the case of curved domains is essential for obtaining even qualitatively correct results.*

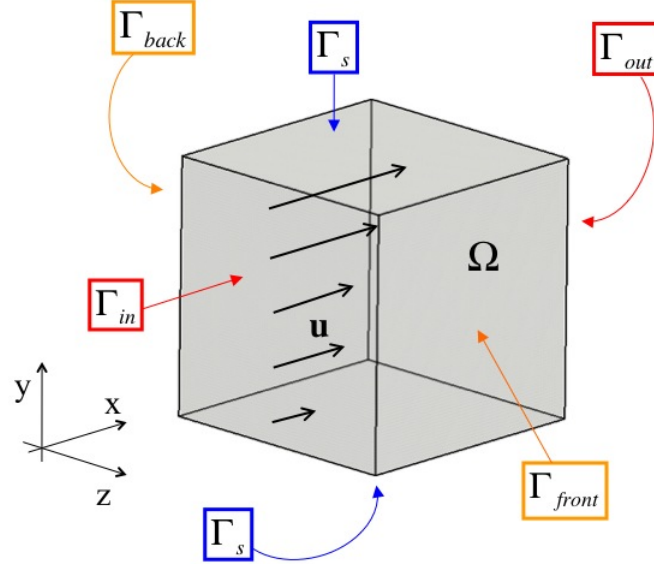


Figure 14: Cube domain, boundaries and shear flow \mathbf{u} .

5.3 Three-dimensional results in a cube

We consider the shear-driven spinodal decomposition in the cube $\Omega = (0, L_0)^3$ depicted in figure 14. We impose periodic boundary conditions on the pairs of faces Γ_{in}/Γ_{out} and $\Gamma_{front}/\Gamma_{back}$ in order to simulate an infinite domain in the flow and transverse directions, and the faces Γ_s are taken to be rigid walls. The advective velocity \mathbf{u} for this problem is exactly the same as for the two-dimensional square domain. In our simulations, we take $\lambda = 1.56 \cdot 10^{-4}$. With this choice, $\mathbb{N}_2 = 6.40 \cdot 10^3$ and $T_0 = 6.40 \cdot 10^3$. Furthermore, using meshes of 80^3 elements satisfies the mesh condition (3.8) for $\tau = 1.0$. We provide numerical results for two cases: (a) $\mathbb{P}e = 10$ and $\bar{c} = 0.5$ and (b) $\mathbb{P}e = 10$ and $\bar{c} = 0.3$.

- (a) In figure 15, we visualize the phase transition for $\mathbb{P}e = 10$ and $\bar{c} = 0.5$ by means of the isosurfaces of c . These isosurfaces correspond to values of $c = 0.35, 0.5, 0.65$ (blue, gray, red). We observe that the solution evolves from an initial perturbed solution to a multi-banded morphology at steady state for which 4 bands, parallel to the solid faces Γ_s , are obtained. We note that the solution evolution appears very similar to that of the square domain. Convergence to steady state at $T = 10^4$ takes 13,594 adaptive time steps for this case.
- (b) In figure 16, we visualize the phase transition for $\mathbb{P}e = 10$ and $\bar{c} = 0.3$. In this case, we observe that the solution evolves from an initial perturbed solution to an intermediate state with 4 tubular structures. Similar results are obtained in [3] at intermediate stages of the simulation of an active Cahn-Hilliard fluid model. Eventually, these four tubular structures break down, and a steady state solution with only one tubular

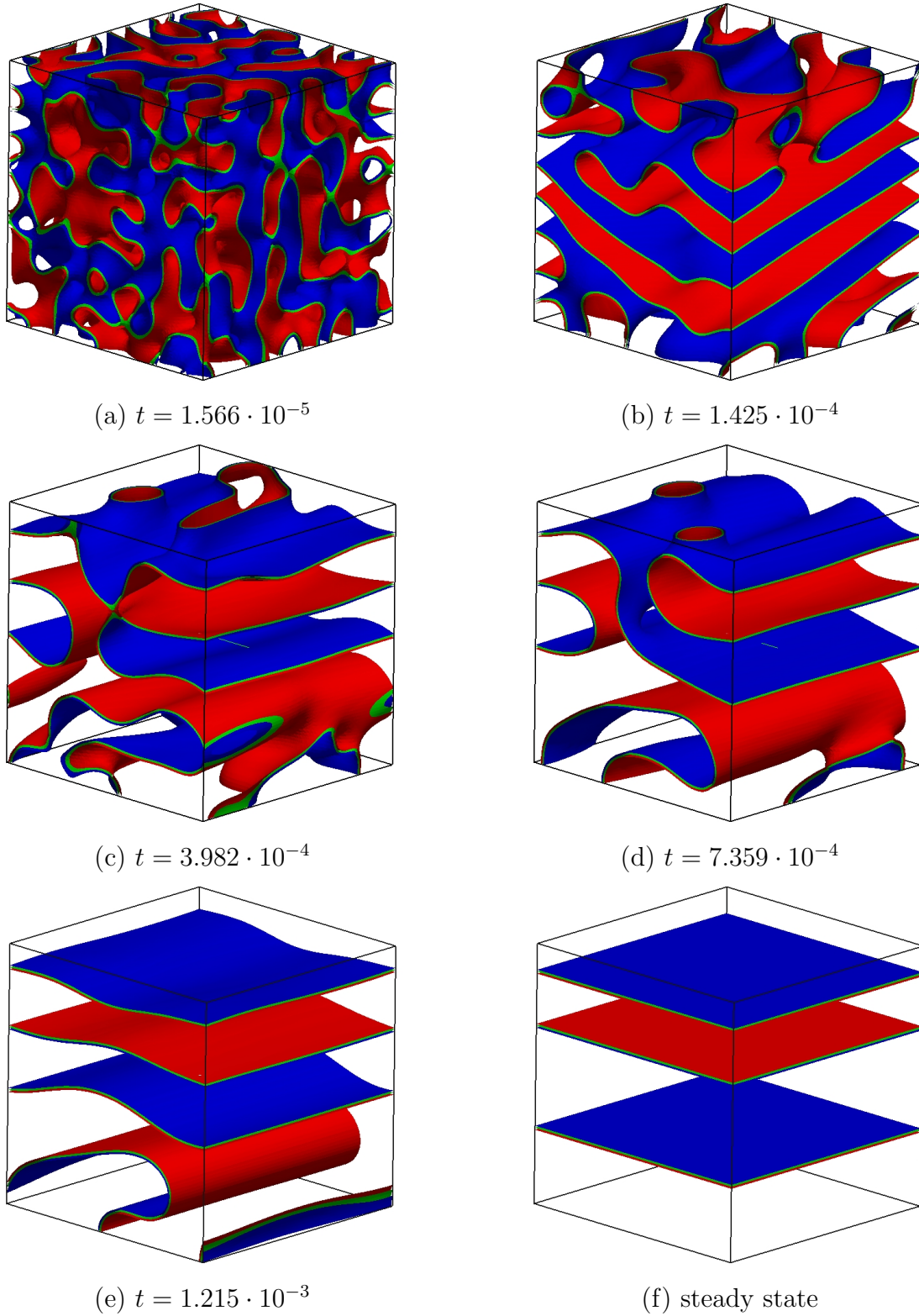


Figure 15: Phase transition in the cube domain for $\mathbb{P}e = 10$ and $\bar{c} = 0.5$.

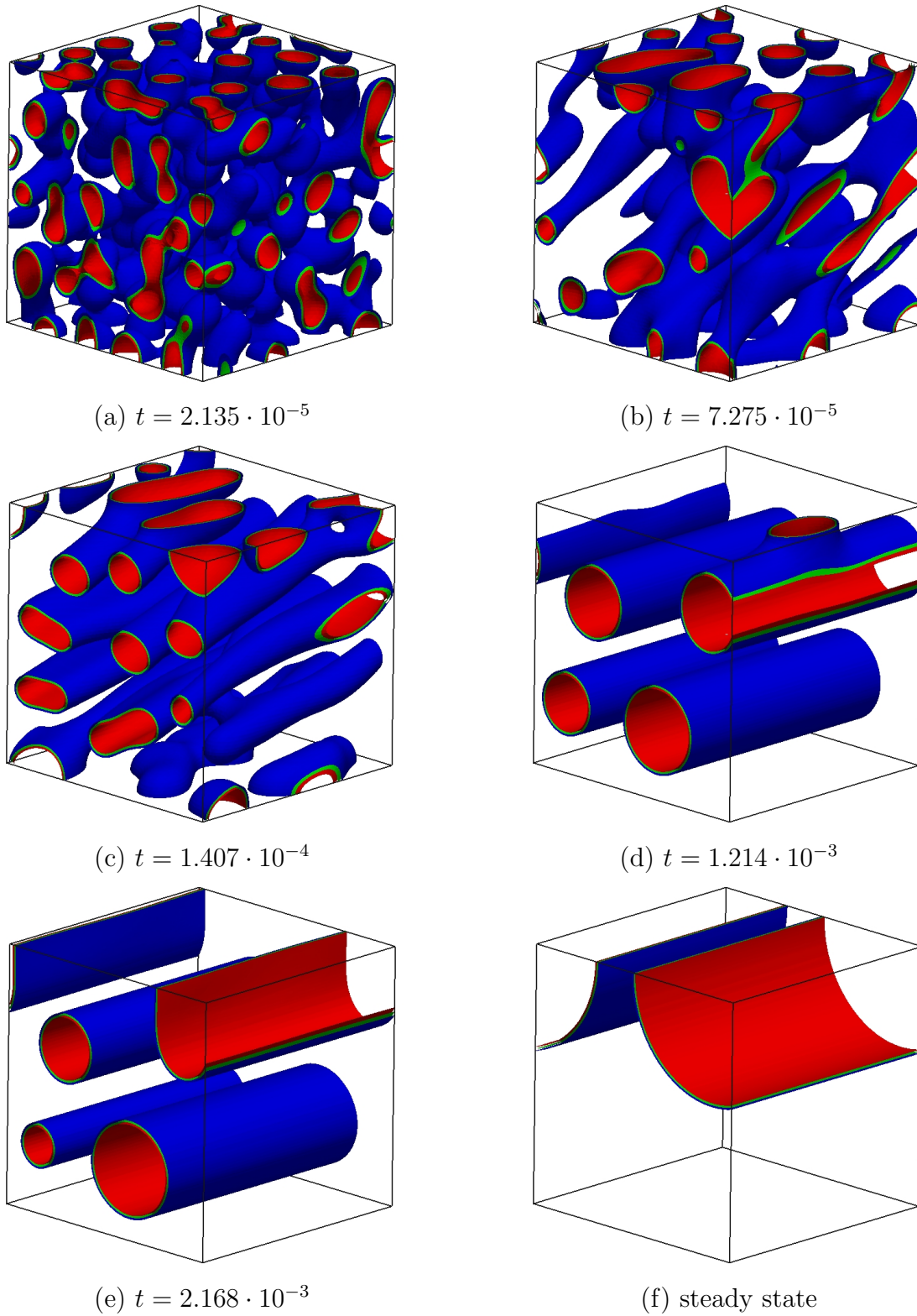


Figure 16: Phase transition in the cube domain for $\mathbb{P}e = 10$ and $\bar{c} = 0.3$.

structure is obtained. We believe this break down is due to an imbalance of surface free energy between the intermediate tubular structures. As these structures have different diameters, they possess different surface free energies, as was the case for the two-dimensional Taylor-Couette cell. Convergence to steady state takes 22,543 adaptive time steps for this case, nearly double the number of time steps required for Case (a).

6 Conclusions

In this paper, we numerically analyzed the spinodal decomposition of a binary fluid undergoing shear flow using the advective Cahn-Hilliard equation and NURBS-based isogeometric analysis. We presented the results of long-time simulations, up to the steady state, in a square domain, a cube domain, and the Taylor-Couette cell, and investigated the effect of shear rate and surface tension on solution evolution. We compared our results for the square domain setting with existing theoretical and experimental results. We developed a new Bézier extraction procedure to enforce periodic boundary conditions in axisymmetric domains. This enabled us to attain accurate response in the case of a Taylor-Couette cell, for which we found the solution of the advective Cahn-Hilliard equation eventually evolves to a two-banded steady state independent of the shear rate. We believe our simulations provide the first numerical evidence of this behavior. Finally, we presented, to the best of our knowledge, the first steady state solutions for three-dimensional shear-driven spinodal decompositions.

Acknowledgements

J. Liu, L. Dedè, J.A. Evans and T.J.R. Hughes were partially supported by the Office of Naval Research under contract number N00014-08-0992. M.J. Borden and T.J.R. Hughes were partially supported by the Army Research Office under contract number W911NF-10-1-0216. M.J. Borden was partially supported by Sandia National Laboratories; Sandia is a multiprogram laboratory operated by Sandia Corporation, a Lockheed Martin Company, for the United States Department of Energy's National Nuclear Security Administration under contract DE-AC04-94AL85000.

The authors also acknowledge the Texas Advanced Computing Center (TACC) at The University of Texas at Austin for providing HPC resources.

A Bézier extraction operator induced by suitable linear transformation

We discuss the modifications on the Bézier data structures induced by the linear transformation of an existing NURBS basis. The notation follows from section 4.

Definition A.1. We call a linear transformation $\bar{\mathbf{T}} \in \mathbb{R}^{n \times n}$, which maps an existing NURBS basis $\mathbf{R}(\xi) := \{R_{A,p}(\xi)\}_{A=1}^n \in \mathbb{R}^n$ to a new NURBS basis $\bar{\mathbf{R}}(\xi) := \{\bar{R}_{A,p}(\xi)\}_{A=1}^n \in \mathbb{R}^n$ by

$$\bar{\mathbf{R}}(\xi) = \bar{\mathbf{T}} \mathbf{R}(\xi), \quad (\text{A.1})$$

suitable if:

- (a) $\bar{\mathbf{T}}$ is invertible,
- (b) $\bar{\mathbf{T}}$ preserves the partition of unity property, i.e.:

$$\bar{\mathbf{T}}^T \mathbf{1} = \mathbf{1}, \quad (\text{A.2})$$

with $\mathbf{1} \in \mathbb{R}^n$ defined as $\mathbf{1} = (1, 1, \dots, 1)^T$.

Since we are in an isogeometric context, it is important that the linear transformation $\bar{\mathbf{T}}$ preserves the geometric mapping. With this aim, the control points associated with the transformed basis $\bar{\mathbf{R}}(\xi)$, $\bar{\mathbf{P}} := \{\bar{\mathbf{P}}_A\}_{A=1}^n \in \mathbb{R}^{n \times d}$, need to be updated accordingly. We have the following proposition.

Proposition A.1. For the linear transformation (A.1), the geometric mapping of the curve $T(\xi) = \sum_{A=1}^n \mathbf{P}_A R_{A,p}(\xi)$ is preserved, if the new control points $\bar{\mathbf{P}} = \{\bar{\mathbf{P}}_A\}_{A=1}^n \in \mathbb{R}^{n \times d}$ are given by:

$$\bar{\mathbf{P}} = \bar{\mathbf{T}}^{-T} \mathbf{P}. \quad (\text{A.3})$$

Proof. The result follows from $T(\xi) = \mathbf{P}^T \mathbf{R}(\xi) = \bar{\mathbf{P}}^T \bar{\mathbf{T}} \mathbf{R}(\xi) = \bar{\mathbf{P}}^T \bar{\mathbf{R}}(\xi)$. \square

To characterize the transformed NURBS basis $\bar{\mathbf{R}}(\xi)$ in terms of the transformation operator $\bar{\mathbf{T}}$ and the Bézier extraction operator of the initial NURBS basis $\mathbf{R}(\xi)$, we introduce the concept of a weighted transformation operator as follows:

Definition A.2. We define the weighted transformation operator $\bar{\mathbf{T}}_{\mathbf{W}} \in \mathbb{R}^{n \times n}$ as:

$$\bar{\mathbf{T}}_{\mathbf{W}} := \mathbf{W}^{-1} \bar{\mathbf{T}} \mathbf{W}, \quad (\text{A.4})$$

where $\mathbf{W} = \text{diag}(\mathbf{w})$ is the diagonal matrix of the weights associated with the basis $\mathbf{R}(\xi)$, and $\bar{\mathbf{T}}$ is given in (A.1).

Lemma A.1. If we denote $\bar{\mathbf{N}}(\xi) = \bar{\mathbf{T}}_{\mathbf{W}} \mathbf{N}(\xi)$, the transformed NURBS basis $\bar{\mathbf{R}}(\xi)$ given in (A.1) could be written as:

$$\bar{\mathbf{R}}(\xi) = \frac{1}{W(\xi)} \mathbf{W} \bar{\mathbf{N}}(\xi), \quad (\text{A.5})$$

and the weight function $W(\xi)$ could be represented as:

$$W(\xi) = \mathbf{w}^T \bar{\mathbf{N}}(\xi). \quad (\text{A.6})$$

Proof. Recall that the definition of $\bar{\mathbf{R}}(\xi)$ is:

$$\bar{\mathbf{R}}(\xi) = \bar{\mathbf{T}} \mathbf{R}(\xi) = \bar{\mathbf{T}} \frac{\mathbf{W}\mathbf{N}(\xi)}{W(\xi)}. \quad (\text{A.7})$$

Then (A.5) follows from the following calculation:

$$\mathbf{W}\bar{\mathbf{T}}\mathbf{w}\mathbf{N}(\xi) = \mathbf{W}\mathbf{W}^{-1}\bar{\mathbf{T}}\mathbf{W}\mathbf{N}(\xi) = \bar{\mathbf{T}}\mathbf{W}\mathbf{N}(\xi). \quad (\text{A.8})$$

(A.6) could be proven by a direct calculation:

$$\mathbf{w}^T \bar{\mathbf{N}}(\xi) = \mathbf{w}^T \mathbf{W}^{-1} \bar{\mathbf{T}} \mathbf{W} \mathbf{N}(\xi) = \mathbf{1}^T \bar{\mathbf{T}} \mathbf{W} \mathbf{N}(\xi) = \mathbf{1}^T \mathbf{W} \mathbf{N}(\xi) = \mathbf{w}^T \mathbf{N}(\xi) = W(\xi). \quad (\text{A.9})$$

The third equality is due to the property (A.2). \square

Since we are interested in the modification of the Bézier data structures due to the linear transformation $\bar{\mathbf{T}}$, we introduce the following relations: the transformed Bézier extraction operator $\bar{\mathbf{C}} \in \mathbb{R}^{n \times (n+m)}$:

$$\bar{\mathbf{C}} := \bar{\mathbf{T}} \mathbf{w} \mathbf{C}, \quad (\text{A.10})$$

with \mathbf{C} being the Bézier extraction operator associated with the NURBS basis $\mathbf{R}(\xi)$; the transformed Bézier weights $\bar{\mathbf{w}}^b \in \mathbb{R}^{n+m}$:

$$\bar{\mathbf{w}}^b := \bar{\mathbf{C}}^T \mathbf{w}, \quad (\text{A.11})$$

with $\bar{\mathbf{W}}^b := \text{diag}(\bar{\mathbf{w}}^b)$ and the weight function: $\bar{W}^b(\xi) := (\bar{\mathbf{w}}^b)^T \mathbf{B}(\xi)$ written in terms of the Bernstein polynomials $\mathbf{B}(\xi)$. The transformed Bézier control points $\bar{\mathbf{P}}^b \in \mathbb{R}^{(n+m) \times d}$ should be:

$$\bar{\mathbf{P}}^b := \left(\bar{\mathbf{W}}^b \right)^{-1} \bar{\mathbf{C}}^T \mathbf{W} \bar{\mathbf{P}}. \quad (\text{A.12})$$

We observe that, following from the definition (A.10), the transformed NURBS basis $\bar{\mathbf{R}}(\xi)$ could be written in terms of the Bernstein polynomials as:

$$\bar{\mathbf{R}}(\xi) = \frac{1}{W(\xi)} \mathbf{W} \bar{\mathbf{C}} \mathbf{B}(\xi). \quad (\text{A.13})$$

Proposition A.2. *For the linear transformation $\bar{\mathbf{T}}$ of definition (A.1), the Bézier weights and control points associated to the transformed NURBS basis $\bar{\mathbf{R}}(\xi)$ are equivalent to those associated to the initial NURBS basis $\mathbf{R}(\xi)$, i.e.:*

$$\bar{\mathbf{w}}^b \equiv \mathbf{w}^b, \quad (\text{A.14})$$

$$\bar{\mathbf{P}}^b \equiv \mathbf{P}^b. \quad (\text{A.15})$$

Proof. We start by proving (A.14) from (A.11). we have the following simple calculation:

$$\overline{\mathbf{w}}^b = \overline{\mathbf{C}}^T \mathbf{w} = \mathbf{C}^T \mathbf{W} \overline{\mathbf{T}}^T \mathbf{W}^{-1} \mathbf{w} = \mathbf{C}^T \mathbf{W} \overline{\mathbf{T}}^T \mathbf{1} = \mathbf{C}^T \mathbf{W} \mathbf{1} = \mathbf{C}^T \mathbf{w}. \quad (\text{A.16})$$

Recall $\mathbf{w}^b = \mathbf{C}^T \mathbf{w}$, which corresponds to the definition of Bézier weights for the basis $\mathbf{R}(\xi)$ given in (4.10). Then (A.14) is proven.

In a similar manner, starting from the definitions (4.11) and (A.12), simple calculations lead to (A.15). \square

In conclusion, the transformed Bézier extraction operator $\overline{\mathbf{C}}$ is the unique Bézier data structure that needs to be modified for the representation of a linearly transformed NURBS basis $\overline{\mathbf{R}}(\xi)$ when starting from an existing NURBS basis $\mathbf{R}(\xi)$. The operator $\overline{\mathbf{C}}$ is completely defined by the transformation operator $\overline{\mathbf{T}}$ and the operator \mathbf{C} . Therefore, it is essential to obtain $\overline{\mathbf{T}}$ for each specific case.

B Periodic transformation operators for NURBS basis

We discuss the periodic transformation operator \mathbf{T}^{per} for NURBS basis functions under a specific but very common hypothesis. In particular, we consider a family of NURBS basis functions $\mathbf{R}(\xi)$ with the following properties:

1. the knot vector $\Xi = \{\xi_i\}_{i=1}^{n+p+1}$ is an open uniform knot vector;
2. the number of knot spans n_{el} has to be greater than or equal to $p + 1$ ($n_{el} \geq p + 1$ or equivalently $n \geq 2p + 1$);
3. the weights $\mathbf{w} \in \mathbb{R}^n$ are symmetric with respect to the knot vector Ξ , i.e. $w_A = w_{n-A+1}$ for all $A = g_n + 1, \dots, n$, with $g_n = n/2$ if n is even or $g_n = (n + 1)/2$ if n is odd²;

Proposition B.1. *Let $\mathbf{N}(\xi) = \{N_{A,p}(\xi)\}_{A=1}^n$ and $\mathbf{R}(\xi) = \{R_{A,p}(\xi)\}_{A=1}^n$ be the B-spline basis and NURBS basis built from the knot vector $\Xi = \{\xi_i\}_{i=1}^{n+p+1}$ and weights $\mathbf{w} = \{w_A\}_{A=1}^n$ satisfying the above hypotheses 1-3. Given the periodic transformation operator \mathbf{T}^{per} which transforms the B-spline basis $\mathbf{N}(\xi)$ to the periodic one $\mathbf{N}^{per}(\xi) = \{N_{A,p}^{per}(\xi)\}_{A=1}^n = \mathbf{T}^{per} \mathbf{N}(\xi)$, then the same periodic transformation operator \mathbf{T}^{per} also transforms the NURBS basis $\mathbf{R}(\xi)$ to the periodic NURBS basis $\mathbf{R}^{per}(\xi) = \{R_{A,p}^{per}(\xi)\}_{A=1}^n$, i.e.: $\mathbf{R}^{per}(\xi) = \mathbf{T}^{per} \mathbf{R}(\xi)$.*

Proof. For simplicity, we prove the result for the case of a globally C^1 -continuous quadratic NURBS basis. Extensions to a general case of p -th degree, C^q -continuous periodic basis with $q \leq p - 1$, can be obtained recursively.

²These requirements can be eventually relaxed and applied only to the starting and ending knots and weights.

For notational simplicity, we assume that the first knot is 0 and the last knot is 1. For a uniform open-knot-vector B-spline basis $\mathbf{N}(\xi) = \{N_i(\xi)\}_{i=1}^n$, we know:

$$\mathbf{N}(0) = (1, 0, \dots, 0)^T, \quad \mathbf{N}(1) = (0, \dots, 0, 1)^T; \quad (\text{B.1})$$

$$\mathbf{N}'(0) = (-d, d, 0, \dots, 0)^T, \quad \mathbf{N}'(1) = (0, \dots, 0, -d, d), \quad (\text{B.2})$$

where d is a nonzero constant. Then for a periodic B-spline basis $\mathbf{N}^{per}(\xi) = \mathbf{T}^{per}\mathbf{N}(\xi)$, we have the following by definition: for $\mathbf{u} = (u_1, \dots, u_n)^T \in \mathbb{R}^n$ satisfying $u_1 = u_{n-1}$ and $u_2 = u_n$, the function $u(\xi) = \mathbf{u}^T\mathbf{N}(\xi)$ is periodic, i.e., $u(0) = u(1)$ and $u'(0) = u'(1)$. Or equivalently we have, for the above vector \mathbf{u} ,

$$\mathbf{u}^T\mathbf{T}^{per}\mathbf{N}(0) = \mathbf{u}^T\mathbf{T}^{per}\mathbf{N}(1), \quad (\text{B.3})$$

$$\mathbf{u}^T\mathbf{T}^{per}\mathbf{N}'(0) = \mathbf{u}^T\mathbf{T}^{per}\mathbf{N}'(1). \quad (\text{B.4})$$

In particular, (B.4) implies:

$$\mathbf{u}^T\mathbf{T}^{per}(-d, d, 0, \dots, 0)^T = \mathbf{u}^T\mathbf{T}^{per}(0, \dots, 0, -d, d)^T \quad (\text{B.5})$$

Due to (B.3), the equality could be written as:

$$\mathbf{u}^T\mathbf{T}^{per}(0, 0, 0, \dots, -d)^T + \mathbf{u}^T\mathbf{T}^{per}(0, d, 0, \dots, 0)^T = \mathbf{u}^T\mathbf{T}^{per}(0, \dots, 0, -d, d)^T \quad (\text{B.6})$$

and we have

$$\mathbf{u}^T\mathbf{T}^{per}(0, d, 0, \dots, 0)^T = \mathbf{u}^T\mathbf{T}^{per}(0, \dots, 0, -d, 2d)^T. \quad (\text{B.7})$$

We notice that for the weight function $W(\xi) = \mathbf{w}^T\mathbf{N}(\xi)$, we have the following facts:

$$W(0) = \mathbf{w}^T\mathbf{N}(0) = w_1 = w_n = \mathbf{w}^T\mathbf{N}(1) = W(1), \quad (\text{B.8})$$

$$W'(0) = \mathbf{w}^T\mathbf{N}'(0) = -dw_1 + dw_2 = -dw_n + dw_{n-1} = -\mathbf{w}^T\mathbf{N}'(1) = -W'(1). \quad (\text{B.9})$$

We show that if \mathbf{T}^{per} is such that $u(0) = u(1)$ and $u'(0) = u'(1)$ for $u_1 = u_{n-1}$ and $u_2 = u_n$, then, for $v(\xi) = \mathbf{v}^T\mathbf{R}^{per}$, we have $v(0) = v(1)$ and $v'(0) = v'(1)$ when $v_1 = v_{n-1}$ and $v_2 = v_n$. Let us choose $\mathbf{v} \in \mathbb{R}^n$ with $v_1 = v_{n-1}$ and $v_2 = v_n$, then

$$\mathbf{v}^T\mathbf{R}^{per}(0) = \mathbf{v}^T\frac{\mathbf{T}^{per}\mathbf{W}\mathbf{N}(0)}{W(0)} = w_1\mathbf{v}^T\frac{\mathbf{T}^{per}\mathbf{N}(0)}{W(1)} = w_1\mathbf{v}^T\frac{\mathbf{T}^{per}\mathbf{N}(1)}{W(1)} \quad (\text{B.10})$$

$$= \mathbf{v}^T\frac{\mathbf{T}^{per}\mathbf{W}\mathbf{N}(1)}{W(1)} = \mathbf{v}^T\mathbf{R}^{per}(1). \quad (\text{B.11})$$

For the first-order derivative, we have by definition:

$$\mathbf{v}^T\mathbf{R}^{per'}(0) = \mathbf{v}^T\mathbf{T}^{per}\mathbf{W}\frac{\mathbf{N}'(0)W(0) - \mathbf{N}(0)W'(0)}{W^2(0)}, \quad (\text{B.12})$$

$$\mathbf{v}^T\mathbf{R}^{per'}(1) = \mathbf{v}^T\mathbf{T}^{per}\mathbf{W}\frac{\mathbf{N}'(1)W(1) - \mathbf{N}(1)W'(1)}{W^2(1)}. \quad (\text{B.13})$$

We have the following derivations by making use of (B.3) and (B.7):

$$\begin{aligned}
\mathbf{v}^T \mathbf{T}^{per} \mathbf{W} \mathbf{N}'(0) &= \mathbf{v}^T \mathbf{T}^{per} (-w_1 d, w_2 d, 0, \dots, 0)^T \\
&= \mathbf{v}^T \mathbf{T}^{per} (-w_1 d, 0, \dots, 0)^T + \mathbf{v}^T \mathbf{T}^{per} (0, w_2 d, \dots, 0)^T \\
&= \mathbf{v}^T \mathbf{T}^{per} (0, \dots, 0, -w_1 d)^T + \mathbf{v}^T \mathbf{T}^{per} (0, \dots, -w_2 d, 2w_2 d)^T \\
&= \mathbf{v}^T \mathbf{T}^{per} (0, \dots, -w_2 d, 2w_2 d - w_1 d)^T.
\end{aligned} \tag{B.14}$$

Then, by making use of (B.1), (B.8), (B.9), and (B.14), (B.12) could be rewritten as:

$$\mathbf{v}^T \mathbf{R}^{per'}(0) = \mathbf{v}^T \mathbf{T}^{per} \frac{w_1(0, \dots, -w_2 d, 2w_2 d - w_1 d)^T + (0, \dots, 0, w_1)^T (dw_1 - dw_2)}{W^2(1)} \tag{B.15}$$

$$= \mathbf{v}^T \mathbf{T}^{per} (0, \dots, 0, -w_2, w_2) \frac{d}{w_1}. \tag{B.16}$$

and (B.13) could be rewritten as:

$$\mathbf{v}^T \mathbf{R}^{per'}(1) = \mathbf{v}^T \mathbf{T}^{per} \frac{w_1(0, \dots, -w_2 d, w_1 d)^T - (0, \dots, 0, w_1)^T (dw_1 - dw_2)}{W^2(1)} \tag{B.17}$$

$$= \mathbf{v}^T \mathbf{T}^{per} (0, \dots, 0, -w_2, w_2) \frac{d}{w_1}. \tag{B.18}$$

Therefore, we have:

$$v(0) = \mathbf{v}^T \mathbf{R}^{per}(0) = \mathbf{v}^T \mathbf{R}^{per}(1) = v(1), \tag{B.19}$$

$$v'(0) = \mathbf{v}^T \mathbf{R}^{per'}(0) = \mathbf{v}^T \mathbf{R}^{per'}(1) = v'(1), \tag{B.20}$$

which complete the proof. \square

As a consequence of Proposition B.1, under the hypotheses 1-3, we can build a periodic transformation operator \mathbf{T}^{per} for a B-spline basis and then use it to transform the NURBS basis to a periodic basis.

C Localized periodic transformation operators

Like the Bézier extraction operator, the periodic transformation operator could be expressed in a localized version. Here we provide the localized periodic transformation operators $\mathbf{T}_e^{per} \in \mathbb{R}^{(p+1) \times (p+1)}$ for a globally p -th degree C^{p-1} -continuous periodic NURBS basis under the hypotheses 1-3 of appendix B:

$$\mathbf{N}_e^{per}(\xi) = \mathbf{T}_e^{per} \mathbf{N}_e(\xi) \quad \text{for } e = 1, \dots, n_{el}, \tag{C.1}$$

with $\mathbf{N}_e^{per}(\xi)$ and $\mathbf{N}_e(\xi) \in \mathbb{R}^{p+1}$ being the B-spline basis functions with support in the e th element. The structure of the localized periodic transformation operator can be obtained

by a knot insertion process [8] and we give its general structure: for \mathbf{T}_e^{per} in the elements $e = 1, \dots, n_{el}$ and $p \geq 1$:

$$\mathbf{T}_e^{per} = \begin{cases} \begin{bmatrix} \alpha_{e,1,1} & 0 & \dots & 0 \\ \vdots & \ddots & \ddots & \vdots \\ \alpha_{e,p,1} & \dots & \alpha_{e,p,p} & 0 \\ 0 & \dots & 0 & 1 \end{bmatrix} & \text{for } e = 1, \dots, p-1, \\ \mathbf{I}_{(p+1) \times (p+1)} & \text{for } e = p, \dots, n_{el} - p + 1, \\ \begin{bmatrix} 1 & 0 & \dots & 0 \\ 0 & \alpha_{n_{el}+1-e,p,p} & \dots & \alpha_{n_{el}+1-e,p,1} \\ \vdots & \ddots & \ddots & \vdots \\ 0 & \dots & 0 & \alpha_{n_{el}+1-e,1,1} \end{bmatrix} & \text{for } e = n_{el} - p + 2, \dots, n_{el}, \end{cases} \quad (\text{C.2})$$

where $\mathbf{I}_{(p+1) \times (p+1)} \in \mathbb{R}^{(p+1) \times (p+1)}$ is the identity matrix.

The coefficients $\alpha_{e,A,B}$ defining \mathbf{T}_e^{per} could be obtained directly by the knot insertion algorithm [8, 49] or by solving a periodic constrained equation. We provide the explicit form of the localized periodic operators \mathbf{T}_e^{per} and \mathbf{C}_e^{per} for NURBS bases of degrees $p = 1, 2$, and 3 under the hypotheses 1-3 of appendix B. We also report the periodic basis $\mathbf{R}^{per}(\xi)$ and control points \mathbf{P}^{per} for a circular arc geometry with degrees $p = 2$ and 3.

C.1 Degree $p = 1$

We have $\mathbf{T}_e^{per} = \mathbf{I}_{2 \times 2}$ for all $e = 1, \dots, n_{el}$, since the basis is already suited to impose C^0 -continuity on the periodic boundaries. This implies that $\mathbf{T}_{\mathbf{w},e}^{per} = \mathbf{I}_{2 \times 2}$ and $\mathbf{C}_e^{per} = \mathbf{C}_e = \mathbf{I}_{2 \times 2}$.

C.2 Degree $p = 2$

For $p = 2$, we impose periodic boundary conditions with continuity of the solution $\widehat{v}_h(\xi)$ up to the first order derivatives. The localized periodic transformation operators $\mathbf{T}_e^{per} \in \mathbb{R}^{3 \times 3}$ read:

$$\mathbf{T}_e^{per} = \begin{cases} \begin{bmatrix} 1/2 & 0 & 0 \\ 1/2 & 1 & 0 \\ 0 & 0 & 1 \end{bmatrix} & \text{for } e = 1, \\ \mathbf{I}_{3 \times 3} & \text{for } e = 2, \dots, n_{el} - 1, \\ \begin{bmatrix} 1 & 0 & 0 \\ 0 & 1 & 1/2 \\ 0 & 0 & 1/2 \end{bmatrix} & \text{for } e = n_{el}, \end{cases} \quad (\text{C.3})$$

and the operators $\mathbf{T}_{\mathbf{w},e}^{per} \in \mathbb{R}^{3 \times 3}$ are:

$$\mathbf{T}_{\mathbf{w},e}^{per} = \begin{cases} \begin{bmatrix} 1/2 & 0 & 0 \\ w_1/(2w_2) & 1 & 0 \\ 0 & 0 & 1 \end{bmatrix} & \text{for } e = 1, \\ \mathbf{I}_{3 \times 3} & \text{for } e = 2, \dots, n_{el} - 1, \\ \begin{bmatrix} 1 & 0 & 0 \\ 0 & 1 & w_1/(2w_2) \\ 0 & 0 & 1/2 \end{bmatrix} & \text{for } e = n_{el}, \end{cases} \quad (\text{C.4})$$

where $\mathbf{w}_e = \{w_i\}_{i=1}^3$ are the weights for $e = 1$ and $\mathbf{w}_e = \{w_i\}_{i=3}^1$ for $e = n_{el}$. The localized Bézier extraction operators $\mathbf{C}_e \in \mathbb{R}^{3 \times 3}$ assume the following forms:

$$\mathbf{C}_e = \begin{cases} \begin{bmatrix} 1 & 0 & 0 \\ 0 & 1 & 1/2 \\ 0 & 0 & 1/2 \end{bmatrix} & \text{for } e = 1, \\ \begin{bmatrix} 1/2 & 0 & 0 \\ 1/2 & 1 & 1/2 \\ 0 & 0 & 1/2 \end{bmatrix} & \text{for } e = 2, \dots, n_{el} - 1, \\ \begin{bmatrix} 1/2 & 0 & 0 \\ 1/2 & 1 & 0 \\ 0 & 0 & 1 \end{bmatrix} & \text{for } e = n_{el}. \end{cases} \quad (\text{C.5})$$

Finally, the localized periodic Bézier extraction operators $\mathbf{C}_e^{per} \in \mathbb{R}^{3 \times 3}$ are:

$$\mathbf{C}_e^{per} = \begin{cases} \begin{bmatrix} 1/2 & 0 & 0 \\ w_1/(2w_2) & 1 & 1/2 \\ 0 & 0 & 1/2 \end{bmatrix} & \text{for } e = 1, \\ \mathbf{C}_e & \text{for } e = 2, \dots, n_{el} - 1, \\ \begin{bmatrix} 1/2 & 0 & 0 \\ 1/2 & 1 & w_1/(2w_2) \\ 0 & 0 & 1/2 \end{bmatrix} & \text{for } e = n_{el}. \end{cases} \quad (\text{C.6})$$

In figure 17 we present an example of a circular arc represented by means of the open-knot-vector basis $\mathbf{R}(\xi)$ and periodic NURBS basis $\mathbf{R}^{per}(\xi)$ with knot vector $\Xi = \{\{0\}_{i=1}^3, 1, 2, \{3\}_{i=1}^3\}$. In this case we have $n = 5$ with $n_{el} = 3$. The control points \mathbf{P} , the periodic control points \mathbf{P}^{per} and weights $\mathbf{w} = \mathbf{w}^{per}$ are³:

$$\mathbf{P} = \begin{bmatrix} 0 & 1 \\ 0.2612 & 1 \\ 0.7346 & 0.7346 \\ 1 & 0.2612 \\ 1 & 0 \end{bmatrix}, \quad \mathbf{P}^{per} = \begin{bmatrix} -0.2612 & 1 \\ 0.2612 & 1 \\ 0.7346 & 0.7346 \\ 1 & 0.2612 \\ 1 & -0.2612 \end{bmatrix}, \quad \mathbf{w} = \begin{bmatrix} 1 \\ 0.9023 \\ 0.8373 \\ 0.9023 \\ 1 \end{bmatrix}. \quad (\text{C.7})$$

³Only 4 decimal digits are reported.

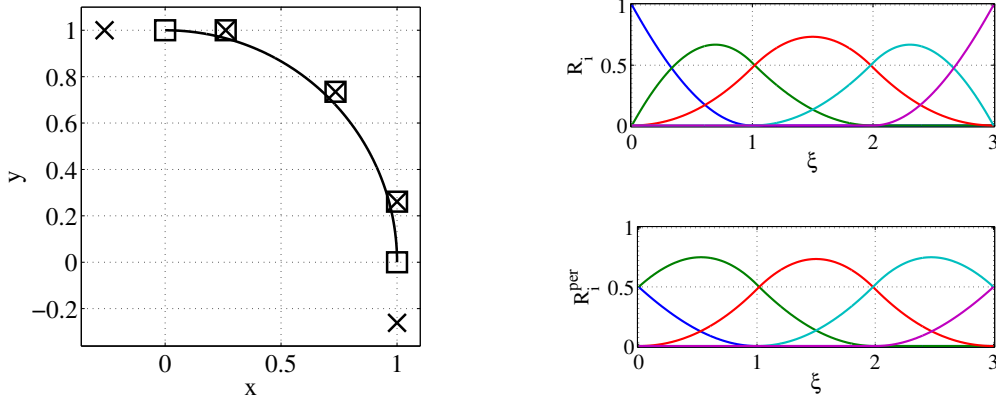


Figure 17: Arc (left) represented by NURBS open-knot-vector (right-top) and periodic (right-bottom) bases of degree $p = 2$; the control points \mathbf{P} (□) and the periodic control points \mathbf{P}^{per} (×) are indicated.

C.3 Degree $p = 3$

For $p = 3$, we impose the periodic boundary conditions with continuity on $\widehat{v}_h(\xi)$ up to second derivatives. The localized operators $\mathbf{T}_e^{per} \in \mathbb{R}^{4 \times 4}$ are:

$$\mathbf{T}_e^{per} = \begin{cases} \begin{bmatrix} 1/6 & 0 & 0 & 0 \\ 2/3 & 2/3 & 0 & 0 \\ 1/6 & 1/3 & 1 & 0 \\ 0 & 0 & 0 & 1 \end{bmatrix} & \text{for } e = 1, \\ \begin{bmatrix} 2/3 & 0 & 0 & 0 \\ 1/3 & 1 & 0 & 0 \\ 0 & 0 & 1 & 0 \\ 0 & 0 & 0 & 1 \end{bmatrix} & \text{for } e = 2, \\ \mathbf{I}_{4 \times 4} & \text{for } e = 3, \dots, n_{el} - 2, \\ \begin{bmatrix} 1 & 0 & 0 & 0 \\ 0 & 1 & 0 & 0 \\ 0 & 0 & 1 & 1/3 \\ 0 & 0 & 0 & 2/3 \end{bmatrix} & \text{for } e = n_{el} - 1, \\ \begin{bmatrix} 1 & 0 & 0 & 0 \\ 0 & 1 & 1/3 & 1/6 \\ 0 & 0 & 2/3 & 2/3 \\ 0 & 0 & 0 & 1/6 \end{bmatrix} & \text{for } e = n_{el}, \end{cases} \quad (\text{C.8})$$

while the operators $\mathbf{T}_{\mathbf{w},e}^{per} \in \mathbb{R}^{4 \times 4}$ are:

$$\mathbf{T}_{\mathbf{w},e}^{per} = \left\{ \begin{array}{ll} \left[\begin{array}{cccc} 1/6 & 0 & 0 & 0 \\ (2w_1)/(3w_2) & 2/3 & 0 & 0 \\ w_1/(6w_3) & w_2/(3w_3) & 1 & 0 \\ 0 & 0 & 0 & 1 \end{array} \right] & \text{for } e = 1, \\ \left[\begin{array}{cccc} 2/3 & 0 & 0 & 0 \\ w_2/(3w_3) & 1 & 0 & 0 \\ 0 & 0 & 1 & 0 \\ 0 & 0 & 0 & 1 \end{array} \right] & \text{for } e = 2, \\ \mathbf{I}_{4 \times 4} & \text{for } e = 3, \dots, n_{el} - 2, \\ \left[\begin{array}{cccc} 1 & 0 & 0 & 0 \\ 0 & 1 & 0 & 0 \\ 0 & 0 & 1 & w_2/(3w_3) \\ 0 & 0 & 0 & 2/3 \end{array} \right] & \text{for } e = n_{el} - 1, \\ \left[\begin{array}{cccc} 1 & 0 & 0 & 0 \\ 0 & 1 & w_2/(3w_3) & w_1/(6w_3) \\ 0 & 0 & 2/3 & (2w_1)/(3w_2) \\ 0 & 0 & 0 & 1/6 \end{array} \right] & \text{for } e = n_{el}, \end{array} \right. \quad (\text{C.9})$$

with the weights $\mathbf{w}_e = \{w_i\}_{i=1}^4$ for $e = 1$, $\mathbf{w}_e = \{w_i\}_{i=2}^5$ for $e = 2$, $\mathbf{w}_e = \{w_i\}_{i=5}^2$ for $e = n_{el} - 1$, and $\mathbf{w}_e = \{w_i\}_{i=4}^1$ for $e = n_{el}$. The localized Bézier extraction operators $\mathbf{C}_e \in \mathbb{R}^{4 \times 4}$ are:

$$\mathbf{C}_e = \left\{ \begin{array}{ll} \begin{bmatrix} 1 & 0 & 0 & 0 \\ 0 & 1 & 1/2 & 1/4 \\ 0 & 0 & 1/2 & 7/12 \\ 0 & 0 & 0 & 1/6 \end{bmatrix} & \text{for } e = 1, \\ \begin{bmatrix} 1/4 & 0 & 0 & 0 \\ 7/12 & 2/3 & 1/3 & 1/6 \\ 1/6 & 1/3 & 2/3 & 2/3 \\ 0 & 0 & 0 & 1/6 \end{bmatrix} & \text{for } e = 2, \\ \begin{bmatrix} 1/6 & 0 & 0 & 0 \\ 2/3 & 2/3 & 1/3 & 1/6 \\ 1/6 & 1/3 & 2/3 & 2/3 \\ 0 & 0 & 0 & 1/6 \end{bmatrix} & \text{for } e = 3, \dots, n_{el} - 2, \\ \begin{bmatrix} 1/6 & 0 & 0 & 0 \\ 2/3 & 2/3 & 1/3 & 1/6 \\ 1/6 & 1/3 & 2/3 & 7/12 \\ 0 & 0 & 0 & 1/4 \end{bmatrix} & \text{for } e = n_{el} - 1, \\ \begin{bmatrix} 1/6 & 0 & 0 & 0 \\ 7/12 & 1/2 & 0 & 0 \\ 1/4 & 1/2 & 1 & 0 \\ 0 & 0 & 0 & 1 \end{bmatrix} & \text{for } e = n_{el}, \end{array} \right. \quad (\text{C.10})$$

for which we obtain the following localized periodic Bézier extraction operators $\mathbf{C}_e^{per} \in \mathbb{R}^{4 \times 4}$:

$$\mathbf{C}_e^{per} = \left\{ \begin{array}{l} \left[\begin{array}{cccc} 1/6 & 0 & 0 & 0 \\ (2w_1)/(3w_2) & 2/3 & 1/3 & 1/6 \\ w_1/(6w_3) & w_2/(3w_3) & (w_2 + 3w_3)/(6w_3) & (w_2 + 7w_3)/(12w_3) \\ 0 & 0 & 0 & 1/6 \end{array} \right] \\ \text{for } e = 1, \\ \\ \left[\begin{array}{cccc} 1/6 & 0 & 0 & 0 \\ (w_2 + 7w_3)/(12w_3) & 2/3 & 1/3 & 1/6 \\ 1/6 & 1/3 & 2/3 & 2/3 \\ 0 & 0 & 0 & 1/6 \end{array} \right] \\ \text{for } e = 2, \\ \\ \mathbf{C}_e \\ \text{for } e = 3, \dots, n_{el} - 2, \\ \\ \left[\begin{array}{cccc} 1/6 & 0 & 0 & 0 \\ 2/3 & 2/3 & 1/3 & 1/6 \\ 1/6 & 1/3 & 2/3 & (w_2 + 7w_3)/(12w_3) \\ 0 & 0 & 0 & 1/6 \end{array} \right] \\ \text{for } e = n_{el} - 1, \\ \\ \left[\begin{array}{cccc} 1/6 & 0 & 0 & 0 \\ (w_2 + 7w_3)/(12w_3) & (w_2 + 3w_3)/(6w_3) & w_2/(3w_3) & w_1/(6w_3) \\ 1/6 & 1/3 & 2/3 & (2w_1)/(3w_2) \\ 0 & 0 & 0 & 1/6 \end{array} \right] \\ \text{for } e = n_{el}. \end{array} \right. \quad (\text{C.11})$$

In figure 18 we present the circular arc obtained with the open-knot-vector basis $\mathbf{R}(\xi)$ and periodic NURBS basis $\mathbf{R}^{per}(\xi)$ with knot vector $\Xi = \{\{0\}_{i=1}^4, 1, 2, 3, \{3\}_{i=1}^4\}$ for which $n = 7$ and $n_{el} = 4$. We have the following control points \mathbf{P} , the periodic control points \mathbf{P}^{per} and weights $\mathbf{w} = \mathbf{w}^{per}$ for the arc³:

$$\mathbf{P} = \begin{bmatrix} 0 & 1 \\ 0.1239 & 1 \\ 0.3830 & 0.9525 \\ 0.7276 & 0.7276 \\ 0.9525 & 0.3830 \\ 1 & 0.1239 \\ 1 & 0 \end{bmatrix}, \quad \mathbf{P}^{per} = \begin{bmatrix} -0.3603 & 0.9525 \\ -0.0057 & 1.0238 \\ 0.3830 & 0.9525 \\ 0.7276 & 0.7276 \\ 0.9525 & 0.3830 \\ 1.0238 & -0.0057 \\ 0.9525 & -0.3603 \end{bmatrix}, \quad \mathbf{w} = \begin{bmatrix} 1 \\ 0.9512 \\ 0.8780 \\ 0.8413 \\ 0.8780 \\ 0.9512 \\ 1 \end{bmatrix}. \quad (\text{C.12})$$

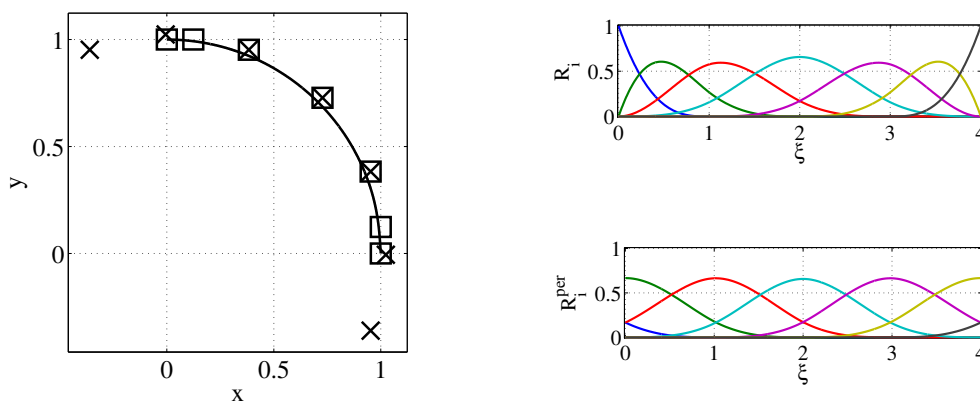


Figure 18: Arc (left) represented by NURBS open-knot-vector (right-top) and periodic (right-bottom) bases of degree $p = 3$; the control points \mathbf{P} (\square) and the periodic control points \mathbf{P}^{per} (\times) are identified.

References

- [1] R.A. Adams. *Sobolev Spaces*. Academic Press, New York, 1975.
- [2] D.M. Anderson, G.B. McFadden, and A.A. Wheeler. Diffuse-interface methods in fluid mechanics. *Annual Review of Fluid Mechanics*, 30:139–65, 1998.
- [3] V.E. Badalassi, H.D. Ceniceros, and S. Banerjee. Computation of multiphase systems with phase field models. *Journal of Computational Physics*, 190:371–397, 2003.
- [4] J.W. Barrett, J.F. Blowey, and H. Garcke. Finite element approximation of the Cahn-Hilliard equation with degenerate mobility. *SIAM Journal on Numerical Analysis*, 37:286–318, 1999.
- [5] Y. Bazilevs, V.M. Calo, J.A. Cottrell, T.J.R. Hughes, A. Reali, and G. Scovazzi. Variational multiscale residual-based turbulence modeling for large eddy simulation of incompressible flows. *Computer methods in Applied Mechanics and Engineering*, 197:173–201, 2007.
- [6] Y. Bazilevs, L.B. Veiga, J.A. Cottrell, T.J.R. Hughes, and G. Sangalli. Isogeometric analysis: approximation, stability and error estimates for h-refined meshes. *Mathematical Models and Methods in Applied Sciences*, 16:1031–1090, 2006.
- [7] C. Blanc and C. Schlick. Accurate Parametrization of Conic by NURBS. *Computer Graphics and Applications*, 16:64–71, 1996.

- [8] M.J. Borden, M.A. Scott, J.A. Evans, and T.J.R. Hughes. Isogeometric finite element data structures based on Bézier extraction of NURBS. *International Journal for Numerical Methods in Engineering*, 87:15–47, 2010.
- [9] F. Boyer. A theoretical and numerical model for the study of incompressible mixture flows. *Computers and Fluids*, 31:41–68, 2002.
- [10] M. Burger, S.Y. Chu, P.A. Markowich, and C.B. Schönlieb. The Willmore functional and instabilities in the Cahn-Hilliard equation. *Communications in Mathematical Science*, 6:309–329, 2008.
- [11] C.K. Cahn, F. Perrot, and D. Beysens. Effects of hydrodynamics on growth: Spinodal decomposition under uniform shear flow. *Physical Review Letters*, 61, 2008.
- [12] J.W. Cahn. On spinodal decomposition. *Acta Metallica*, 9:795–801, 1961.
- [13] J.W. Cahn and J.E. Hilliard. Free energy of a nonuniform System. I. Interfacial free energy. *Journal of Chemical Physics*, 28:258–267, 1958.
- [14] J.W. Cahn and J.E. Hilliard. Free energy of a nonuniform system. III. Nucleation in a two-component incompressible fluid. *Journal of Chemical Physics*, 31:688–699, 1959.
- [15] L.Q. Chen. Phase-field models for microstructure evolution. *Annual Review of Material Research*, 32:113–140, 2002.
- [16] X. Chen, L. Niu, and H. Shi. Numerical simulation of the phase separation in binary lipid membrane under the effect of stationary shear flow. *Biophysical Chemistry*, 135:84–94, 2008.
- [17] J. Chung and G.M. Hulbert. A time integration algorithm for structural dynamics with improved numerical dissipation: The generalized- α method. *Journal of Applied Mechanics*, 60:371–375, 1993.
- [18] J.A. Cottrell, T.J.R. Hughes, and Y. Bazilevs. *Isogeometric Analysis: Towards Integration of CAD and FEA*. John Wiley and Sons, 2009.
- [19] J.A. Cottrell, T.J.R. Hughes, and A. Reali. Studies of refinement and continuity in Isogeometric structural analysis. *Computer Methods in Applied Mechanics and Engineering*, 196:4160–4183, 2007.
- [20] L. Cueto-Felgueroso and J. Peraire. A time-adaptive finite volume method for the Cahn-Hilliard and Kuramoto-Sivashinsky equations. *Journal of Computational Physics*, 227:9985–10017, 2008.
- [21] L. Dedè, M.J. Borden, and T.J.R. Hughes. Isogeometric analysis for topology optimization problems in a phase field approach. Technical Report 11-29, Institute for Computational Engineering and Sciences, The University of Texas at Austin, 2011.

- [22] D. Derks, D.G.A.L. Aarts, D. Bonn, and A. Imhof. Phase separating colloid polymer mixtures in shear flow. *Journal of Physics: Condensed Matter*, 20:412–416, 2008.
- [23] H. Ding, P.D.M. Spelt, and C. Shu. Diffuse interface model for incompressible two-phase flows with large density ratios. *Journal of Computational Physics*, 226:2078–2095, 2007.
- [24] C.M. Elliott, D.A. French, and F.A. Milner. A 2nd-order splitting method for the Cahn-Hilliard equation. *Numerische Mathematik*, 54:575–590, 1989.
- [25] C.M. Elliott and H. Garcke. On the Cahn-Hilliard equation with degenerate mobility. *SIAM Journal on Mathematical Analysis*, 27:404–423, 1996.
- [26] C.M. Elliott and Z. Songmu. On the Cahn-Hilliard equation. *Archive for Rational Mechanics and Analysis*, 96:339–357, 1986.
- [27] G. Engel, K. Garikipati, T.J.R. Hughes, M.G. Larson, L. Mazzei, and R.L. Taylor. Continuous/discontinuous finite element approximations of fourth-order elliptic problems in structural and continuum mechanics with applications to thin beams and plates, and strain gradient elasticity. *Computer Methods in Applied Mechanics and Engineering*, 191:3669–3750, 2002.
- [28] J.A. Evans, Y. Bazilevs, I. Babuska, and T.J.R. Hughes. n-Widths, sup-infs, and optimality ratios for the k-version of the isogeometric finite element method. *Computer Methods in Applied Mechanics and Engineering*, 198:1726–1741, 2009.
- [29] P.C. Fife. Models for phase separation and their mathematics. *Electronic Journal of Differential Equations*, 48:1–26, 2000.
- [30] K. Fujioka, T. Takebe, and T. Hashimoto. Shear-induced homogenization of semidilute solution of polymer mixture II. Composition dependence. *Journal of Chemical Physics*, 98:717–729, 1992.
- [31] H. Gómez, V.M. Calo, Y. Bazilevs, and T.J.R. Hughes. Isogeometric analysis of the Cahn-Hilliard phase-field model. *Computer Methods in Applied Mechanics and Engineering*, 197:4333–4352, 2008.
- [32] H. Gómez and T.J.R. Hughes. Provably unconditionally stable, second-order time accurate, mixed variational methods for phase-field models. *Journal of Computational Physics*, 230:45310–5327, 2011.
- [33] H. Gómez, T.J.R. Hughes, X. Nogúeira, and V.M. Calo. Isogeometric analysis of the Navier-Stokes-Korteweg equations. *Computer Methods in Applied Mechanics and Engineering*, 199:1828–1840, 2010.
- [34] M.E. Gurtin, D. Polignone, and J. Vinals. Two-phase binary fluids and immiscible fluids described by an order parameter. *Mathematical Models and Methods in Applied Sciences*, 6, 1996.

- [35] T. Hashimoto, K. Matsuzaka, E. Moses, and A. Onuki. String phase in phase-separating fluids under shear flow. *Physical Review Letters*, 74:126–129, 1995.
- [36] A.J. Hawkins-Daarud. *Toward a predictive model of tumor growth*. PhD thesis, The University of Texas at Austin, 2011.
- [37] D.Q. He and E. B. Nauman. On spinodal decomposition of binary polymer blends under shear flows. *Chemical Engineering Science*, 52:481–496, 1997.
- [38] L.P. He and Y. Liu. A class of stable spectral methods for the Cahn-Hilliard equation. *Journal of Computational Physics*, 228:5101–5110, 2009.
- [39] Y. He, Y. Liu, and T. Tang. On large time-stepping methods for the Cahn-Hilliard equation. *Applied Numerical Mathematics*, 57:616–628, 2007.
- [40] T.J.R. Hughes. *The Finite Element Method: Linear Static and Dynamic Finite Element Analysis*. Dover Publications, Mineola, NY, 2000.
- [41] T.J.R. Hughes, J.A. Cottrell, and Y. Bazilevs. Isogeometric analysis: CAD, finite elements, NURBS, exact geometry and mesh refinement. *Computer Methods in Applied Mechanics and Engineering*, 194:4135–4195, 2005.
- [42] D. Jacqmin. Calculation of two-phase Navier-Stokes flows using phase-field modeling. *Journal of Computational Physics*, 155:96–127, 1999.
- [43] D. Jamet, O. Lebaigue, N. Coutris, and J.M. Delhaye. The second gradient method for the direct numerical simulation of liquid-vapor flows with phase change. *Journal of Computational Physics*, 169:624–651, 2001.
- [44] K.E. Jansen, C.H. Whiting, and G.M. Hulbert. A generalized- α method for integrating the filtered Navier-Stokes equations with a stabilized finite element method. *Computer Methods in Applied Mechanics and Engineering*, 190:305–319, 2000.
- [45] S. Lipton, J.A. Evans, Y. Bazilevs, T. Elguedj, and T.J.R. Hughes. Robustness of Isogeometric structural discretizations under severe mesh distortion. *Computer Methods in Applied Mechanics and Engineering*, 199:357–373, 2009.
- [46] J. Lowengrub and L. Truskinovsky. Quasi-incompressible Cahn-Hilliard fluids and topological transitions. *Proceedings of the Royal Society A*, 454:2617–2654, 1998.
- [47] L. Modica. The gradient theory of phase transitions and the minimal interface criterion. *Archive for Rational Mechanics and Analysis*, 98:123–142, 1987.
- [48] L.O. Naraigh and J. Thiffeault. Bubbles and filaments: Stirring a Cahn-Hilliard fluid. *Physical Review E*, 75:016216.1–016216.11, 2007.
- [49] L. Piegl and W. Tiller. *The NURBS Book*. Springer-Verlag, New York, 1997.

- [50] A. Quarteroni, R. Sacco, and F. Saleri. *Numerical Mathematics*. Springer-Verlag, Berlin, 2007.
- [51] Y. Saad and M.H. Schultz. GMRES: A generalized minimal residual algorithm for solving nonsymmetric linear systems. *SIAM Journal of Scientific and Statistical Computing*, 7:856–869, 1986.
- [52] O. Soriano-Vargas, E.O. Avila-Davila, V.M. Lopez-Hirata, N.Cayetano-Castro, and J.L. Gonzales-Velazquez. Effect of spinodal decomposition on the mechanical behavior of Fe–Cr alloys. *Material Science and Engineering A*, 527:2910–2914, 2010.
- [53] R.H. Stogner and G.F. Carey. C^1 macroelements in adaptive finite element methods. *International Journal for Numerical Methods in Engineering*, 70:1076–1095, 2007.
- [54] K. Stratford, J.-C. Desplat, P. Stansell, and M.E. Cates. Binary fluids under steady shear in three dimensions. *Physical Review E*, 76, 2007.
- [55] A. K. Thakre, W.K. den Otter, J.T. Padding, and W.J. Briels. Spinodal decomposition of asymmetric binary fluids in a micro-Couette geometry simulated with molecular dynamics. *The Journal of Chemical Physics*, 129, 2008.
- [56] K.G. van der Zee, J. Tinsley Oden, S. Prudhomme, and A. Hawkins-Daarud. Goal-oriented error estimation for Cahn-Hilliard models of binary phase transition. *Numerical Methods for Partial Differential Equations*, 27:160–196, 2011.
- [57] A. J. Wagner and J. M. Yeomans. Phase separation under shear in two-dimensional binary fluids. *Physical Review E*, 59:4366–4373, 1999.
- [58] G.N. Wells, E. Kuhl, and K. Garikipati. A discontinuous Galerkin method for the Cahn-Hilliard equation. *Journal of Computational Physics*, 218:860–877, 2006.
- [59] O. Wodo and B. Ganapathysubramanian. Computationally efficient solution to the Cahn-Hilliard equation: Adaptive implicit time schemes, mesh sensitivity analysis and the 3D isoperimetric problem. *Journal of Computational Physics*, 230:6037–6060, 2011.
- [60] P. Yue, J. J. Feng, C. Liu, and J. Shen. A diffuse-interface method for simulating two-phase flows of complex fluids. *Journal of Fluid Mechanics*, 515:293–317, 2004.